

DEVELOPMENT OF PRINTABLE CONCRETE MIX USING ML MODELS

M.Tech Thesis

By

ADITYA BHANDAKKAR

(2302104010)



**DEPARTMENT OF CIVIL ENGINEERING
INDIAN INSTITUTE OF TECHNOLOGY
INDORE**

May 2025

DEVELOPMENT OF PRINTABLE CONCRETE MIX USING ML MODELS

A THESIS

*Submitted in partial fulfillment of the
requirements for the award of the degree
of
Master of Technology
(2023-2025)*

STRUCTURAL ENGINEERING

By

ADITYA BHANDAKKAR
(2302104010)

*Under Guidance
of*

Dr. Abhishek Rajput
(Associate Professor)



**DEPARTMENT OF CIVIL ENGINEERING
INDIAN INSTITUTE OF TECHNOLOGY
INDORE**

May 2025




INDIAN INSTITUTE OF TECHNOLOGY INDORE


CANDIDATE'S DECLARATION

I hereby certify that the work which is being presented in the thesis entitled **DEVELOPMENT OF PRINTABLE CONCRETE MIX USING ML MODELS** in the partial fulfillment of the requirements for the award of the degree of **MASTER OF TECHNOLOGY** and submitted in the **DEPARTMENT OF CIVIL ENGINEERING, INDIAN INSTITUTE OF TECHNOLOGY INDORE**, is an authentic record of my own work carried out during the time period from **JUNE 2023** to **MAY 2025** under the supervision of Dr. Abhishek Rajput, Associate Professor, Department of Civil Engineering, Indian Institute of Technology, Indore.

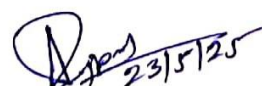
The matter presented in this thesis has not been submitted by me for the award of any other degree of this or any other institute.



Aditya Bhandakkar
Date: 23/05/2025

This is to certify that the above statement made by the candidate is correct to the best of my/our knowledge.


Signature of the Supervisor of M.Tech. Thesis -**Dr. Abhishek Rajput**
Date: -----

Aditya Bhandakkar has successfully given his M.Tech. Oral Examination held on **09th May 2025**.


Signature of Supervisor of M.Tech. Thesis:
Date: -----


Convener, DPCG
Date: May 27, 2025.

ACKNOWLEDGEMENTS

I would like to express my profound gratitude to my M.Tech. Project Supervisor and Head of the Department, Dr. Abhishek Rajput, as well as to the Director, Prof. Suhas Joshi, for granting me the invaluable opportunity to work on this project. Their unwavering support and expert guidance have enabled me to explore a compelling research topic, engage in comprehensive studies, and significantly enhance my skills. This project has not only deepened my academic knowledge but also contributed significantly to my personal and professional development. I am deeply appreciative of their continuous encouragement and mentorship throughout this endeavour.

Additionally, I extend my sincere thanks to Mr. Manish Yadav, a Ph.D. scholar in the Department of Civil Engineering, for his invaluable support and collaboration. Together with Dr. Abhishek Rajput, he has cultivated an environment conducive to critical thinking and research excellence. Their consistent availability for discussions, clarity on complex issues, and overall guidance at every phase of this project have been instrumental in its successful completion. Their encouragement in addressing challenges encountered during the research, as well as their mentorship in broader life and career matters, is greatly appreciated.

ABSTRACT

The technique of three-dimensional (3D) concrete printing (3DCP) has emerged as a highly advanced construction method, attracting considerable attention in recent times. Machine learning (ML) models are employed in this study to predict the most effective mix designs for 3D-printable concrete (3DPC). By analyzing various data inputs, these models help identify the optimal mix proportions that would ensure the best performance in 3D concrete printing. The approach also predicts the compressive strength (CS) of 3D printed materials. Five ML models are utilized in this study: Random forest (RF), Support vector machine (SVM), Extreme Gradient boosting (XGBoost), Decision Tree (DT), and Gradient boosting machine (GBM). The compressive strength data were collected for 150 research papers, and with a mix design of over 500. Hyper-parameter optimization techniques are used to optimize the parameters of the ML models. On CS, the accuracy is approximately $R^2 = 0.82, 0.81, 0.80$. The SHAP analysis detects that water/binder (W/B) ratio and ordinary Portland cement content are the most effective parameters for CS. The ML models incorporated with SHAP analysis disclose the relationship between the input variables and the mechanical performance of 3DCP. They could provide valuable information for the performance-based design of the mix proportion of 3DCP. The amount of clay and silica fumes also influences the properties, such as buildability. The VMA and SP are influential parameters in extrudability. In this paper, the compression test is performed on every direction of layers, i.e., perpendicular to printing direction, parallel to printing direction in X axis, and parallel to printing direction in Y axis. The compressive strength values for various loads provide the best loading direction plane inputs

TABLE OF CONTENTS

Chapters	List of Contents	Page number
	List of figures	ii-ii
	List of tables	ii
Chapter 1	INTRODUCTION	1 - 3
1.1	Introduction to 3D Concrete Printing (3DCP) and Its Significance	1
1.2	Evolution of 3D Concrete Printing and Current Trends	1
1.3	Machine Learning in 3D Concrete Printing: Role and Potential	2
1.4	Data-Driven Analysis and Multi-Objective Optimization in 3DCP	2
1.5	ML Applications in 3D Concrete Printing	3
Chapter 2	LITERATURE REVIEW	4 - 12
2.1	General	4
2.2	Overview of 3D Printable Concrete	4
2.3	Traditional Approaches to Mix Design	5
2.4	Machine Learning in 3D Concrete Printing	5
2.5	ML Applications in 3D Concrete Printing	6

2.6	Explainable Artificial Intelligence (XAI) in Concrete Modelling	8
2.7	Properties of 3D Concrete Printing	9
2.8	Rheology of cementitious system	10
2.9	Identified Research Gaps	12
Chapter 3	METHODOLOGY	13 - 31
3.1	AI and ML Models used in predicting mix designs	13
3.1.1	XGBoost	13
3.1.2	Support Vector Machine	16
3.1.3	Random Forest	18
3.1.4	Decision Tree	20
3.1.5	Artificial Neural Network	21
3.2	AI and ML Models used in predicting mix designs	22
3.3	Data Collection and Analysis	23
3.4	Materials and Methods	25
3.5	Correlation Matric	26
3.6	Prediction and Evaluation of ML Model Performance	28
3.7	SHAP for Compressive Strength	30
Chapter 4	EXPERIMENTATION OF 3DCP	31 - 35
4.1	General	31

4.2	3D Printer Platform Calibration	32
4.3	Test Bed Printer and Its Calibration	33
4.4	Test Bed	33
4.5	Pump integrated 3D Concrete Mixer	34
Chapter 5	MIX PROPORTIONS, TESTS AND CONCRETE PRINTING	36 -55
5.1	General	36
5.2	Components of 3DCP Mix	37
5.3	Mixing Process for 3D Concrete Printable Mix	40
5.4	Printing Tests	42
5.4.1	Extrudability Test	43
5.4.2	Buildability Test	44
5.4.3	Open Time Test	47
5.5	Mix Proportions of the Studied Trial	50
5.6	Preparation of Test Specimen	51
5.7	Mechanical Properties Test and Results	54
5.7.1	Compression Strength Test	53
5.7.2	Flexure Strength Test	54
Chapter 6	RESULTS AND DISCUSSION	56 - 92
6.1	Fresh 3DCP Mix Design	56
6.2	Predictions by ML Models	58

6.3 Mechanical Test Results	59
Chapter 7 FUTURE SCOPE	62
Chapter 8 REFERENCES	63 -71

LIST OF FIGURES

Figure no.	Title of Figure	Page Number
1.	Flow chart of DT (Taken from Huaxing gao, Lang jin et al.)	6
2.	Flow chart of RF (Taken from Huaxing gao, Lang jin et al)	6
3.	Flow chart of XGBoost (Taken from Huaxing gao, Lang jin et al)	6
4.	Flow chart of ANN (Taken from Huaxing gao, Lang jin et al)	6
5.	Strain sweep test on a cement paste sample ((taken from Qian and Kawashima (2016)	9
6.	Creep test at different stress levels on a cement paste sample (taken from Qian and Kawashima (2016)	9
7.	Illustration of the XGBoost Model	16
8.	Illustration of the Support Vector Machine Model	18
9.	Illustration of the Random	19
10.	Illustration of the Decision Tree	20
11.	Illustration of ANN	21
12.	Variation of Mix Design Components in 3D Printable concrete	23
13.	Scatter Plot Diagram of Mix design for 10 input variables	24
14.	Correlation Matrix	26
15.	Comparison of ML Model (ANN)	27

16.	Comparison of ML Models(GBM	27
17.	Comparison of ML Model performance-Compact RF	27
18.	Comparison of ML Model performance- DT	27
19.	Comparison of ML Model performance - GBM	27
20.	Comparison of ML Model performance- RF	27
21.	Comparison of ML Model performance- SVM	27
22.	RMSE/MAE Performance value for compressive strength	29
23.	MAE Performance values - Compressive Strength	29
24.	RMSE Performance values - Compressive Strength	29
25.	SHAP analysis for the 3D printable mix design	30
26.	SHAP analysis for the 3D printable mix design	31
27.	Gantry based 3DCP, POD, IIT Indore	33
28.	Pump integrated material mixer -3DCP. POD, IIT Indore	34
29.	Extrusion Speed (V1) and Printing speed (V2)	36
30.	Extruded layers with uniform thickness and Height	36
31.	Flow diagram showing the printing process	36
32.	Real-time properties of 3DCP	43
33.	Illustrate Extrudability- PASS (Smooth surface and continuous print)	44
34.	Illustrate Extrudability- FAIL (Contains lots of voids and defects)	44

35.	illustration of Buildability Test- Same width of Layers	46
36.	Illustrate image for Buildability- PASS (Smooth surface and continuous print)	47
37.	Illustrate image for Buildability- PASS (Smooth surface and continuous print)	47
38.	Illustrate image for Buildability- FAIL (Not Extrudable slump, Stiff	47
39.	Illustrate image for Buildability- FAIL (Overflow and collapsible slump)	47
40.	End of open time with interruption and rough surface of filaments after 2min of printing	49
41.	Cutting of slab into cubes- 50x50x50mm	52
42.	Cutting of slab in beam- 160x40x40mm	52
43.	Flow chart of the samples making procedure	52
44.	Schematic diagram for the steps to carried out during 3D concrete printing	53
45.	Sample CSZX01	54
46.	Sample FSZX01	54

LIST OF TABLES

Sr. No.	Title of Table	Page Number
1	Prediction and Evaluation of ML Model Performance	28
2	Mix Proportions of Studied Trial	51
3	Compression Test Results	55
4	Flexure Test Results	56

Chapter 1

Introduction

1.1 Introduction to 3D Concrete Printing (3DCP) and Its Significance

The application of 3D printing technology in the construction sector has emerged as an innovative approach to address a number of industrial problems. Conventional methods of concrete fabrication are often labor-intensive, demanding significant resources for manual mixing and casting, leading to considerable material waste. These traditional techniques are inefficient and significantly add to the environmental impact of construction projects. To address these challenges, 3D printing has emerged as a cutting-edge solution that can enhance productivity, minimize waste, and provide notable cost savings. Research indicates that 3D printed concrete can reduce the 30 to 60 percent material waste, drop labour expenses by 50 to 80 percent, and accelerate fabrication time by 50 to 70 percent. The capability to construct buildings layer by layer with a 3D printer has enabled the creation of large concrete structures, such as apartment complexes and bridges, highlighting the expanding possibilities of this technology.

1.2 Evolution of 3D Concrete Printing and Current Trends

3D concrete printing first gained attention in the mid-1990s and has since evolved significantly. The process involves mixing and pumping concrete through a nozzle, where its pumpability and cohesiveness are crucial to ensuring smooth extrusion and structural integrity upon deposition. Over the years, several large-scale structures have been successfully constructed using 3D-printed concrete, and countries like the United States, China, the UK, and Germany are leading the charge in advancing this technology. As

3DCP gains traction, ongoing efforts focus on optimizing material properties and developing accurate material models to predict the behavior of concrete mixtures, essential for further scaling the technology and ensuring its feasibility in various construction applications.

1.3 Machine Learning in 3D Concrete Printing: Role and Potential

As the sector of 3D concrete printing progresses, one of the primary focuses is on the development of material models that can predict the behavior of concrete mixtures. A key property being investigated is compressive strength, which is closely associated with other mechanical properties like tensile and flexural strength. Traditional methods based on experimental data face challenges due to the complex, nonlinear relationships inherent in 3D-printed concrete. To address these challenges, machine learning (ML) models are being increasingly applied to predict and optimize the performance of concrete mixtures. By utilizing large datasets and advanced algorithms, such as artificial neural networks (ANN), support vector machines (SVM), and decision trees, machine learning offers a more accurate, data-driven approach to predicting the mechanical properties of 3D-printed concrete, reducing the reliance on trial-and-error testing.

1.4 Data-Driven Analysis and Multi-Objective Optimization in 3DCP

The paper by Schossler et al. (2025) highlights the use of machine learning to optimize 3D concrete printing (3DCP) mixtures. It integrates a large, comprehensive dataset from 32 different studies, ensuring that the models are generalizable across various 3DCP compositions. A key strength of this study is the use of Bayesian optimization for hyperparameter tuning and

tenfold cross-validation, which rigorously validates the models and mitigates the risk of overfitting. The study incorporates traditional performance metrics, such as compressive strength and pump speed, alongside sustainability metrics, like carbon footprint, providing a multi-objective perspective that aligns well with current construction sustainability goals. The application of SHAP (Shapley Additive Explanations) further enhances the transparency of the model, making it not just accurate but interpretable for industrial applications.

1.5. Limitations and Future Directions in 3DCP Research

Despite its robust technical methodology, the study by Schossler et al. (2025) has some limitations. The paper assumes the adequacy of the compiled literature-based dataset without addressing potential inconsistencies in experimental conditions across the different studies, such as variations in curing methods or machine parameters. Such differences could introduce biases, affecting the model's generalizability. Furthermore, while the study focuses on regression tasks (predicting numerical values), it does not explore classification tasks, such as predicting the success or failure of printability or categorizing the performance of mixtures. Additionally, while the multi-objective optimization (using **NSGA-II**) is well-executed computationally, the practical feasibility of the suggested optimal mixtures has not been experimentally validated. Closing the gap between computational predictions and real-world experimental validation is a key avenue for future research in 3DCP.

Chapter 2

Literature Review

2.1 General

In this section, a thorough literature review and the necessity for this research are discussed. At first the review of AI and ML models that are used in this research is described. The different ML models and their background derivations are presented. This is followed by an explanation of the printable mix designs suggestions. Based on the suggestion of the mix design predicted by the machine learning is explained. Following that, various methods for assessing the physical properties of concrete paste are discussed. Based on the literature review conducted, the necessity of the 3D digital construction is explained in the last subsection section of this chapter.

2.2 Overview of 3D Printable Concrete

3D printable concrete (3DPC) is an advanced construction material enabling **layer-by-layer deposition without formwork**, significantly reducing labor and material waste while offering architectural freedom. However, this technology presents new challenges, particularly in achieving required **rheological and mechanical performance** during and after printing.

Key fresh-state properties for printability include:(Rahul et al., 2019a)

- **Extrudability:** Ability to be continuously extruded through a nozzle.
- **Buildability:** Capability to hold its shape upon deposition without collapse.

- **Open time:** Duration the mix remains printable after mixing.
- **Interlayer bonding strength:** Affects structural integrity between printed layers.
- These parameters are governed by rheological behavior, particularly **yield stress**, **plastic viscosity**, and **thixotropy**. Ma et al. introduced a multi-step mix design method that first ensures extrudability by adjusting SCMs and fibers, followed by balancing buildability and strength via admixtures like superplasticizers. Static yield stress described by the Rahul et al., 2019b in 1.5 to 2.5kpa range. This yield stress has been identified as optimal for both extrudability and buildability.

2.3 Traditional Approaches to Mix Design

Traditional 3DPC mix design methods are based on empirical procedures like **slump flow**, **rheological tests**, and **trial batching**(Rahul et al., 2019a, 2019c). demonstrated that yield stress-driven formulations are more effective in targeting printability. They found that incorporating silica fume and nano clay enhanced both stability and extrudability. (Liu et al., 2022a). used a **multi-objective optimization** approach to correlate SCM content (fly ash, silica fume) with rheological properties, guiding systematic mix development. The **Fuller-Thompson and Marson-Percy models**, traditionally used for optimizing packing density in concrete, were adapted to improve 3DPC printability through enhanced aggregate gradation control.Despite these advances, traditional methods remain limited due to high **dependency on physical testing** and the **nonlinear nature** of material interactions.

2.4 Machine Learning in 3D Concrete Printing

Machine learning (ML) addresses these limitations by modeling complex, nonlinear relationships in concrete compositions. (Ghasemi & Naser, 2023) compiled **307 samples from 53 sources** to train **Random Forest**,

XGBoost, and Multilinear Regression models for predicting compressive strength of 3DPC. Their Random Forest model achieved $R^2 = 0.846$, outperforming other techniques.

- Cement
- Water
- Fly ash
- Silica fume
- Fine aggregate
- Superplasticizer
- Age

Cross-validation (5-fold, repeated twice) and metrics like **MAE**, **MSE**, and **RMSE** were used for evaluation. These findings highlight ML's ability to **replace or augment trial-based design**, making it suitable for high-dimensional optimization.. (Izadgoshasb et al., 2021) proposed a hybrid ML model combining **Artificial Neural Network (ANN)** with **Multi-Objective Grasshopper Optimization Algorithm (MOGOA)** to enhance the strength prediction of printed mortars.

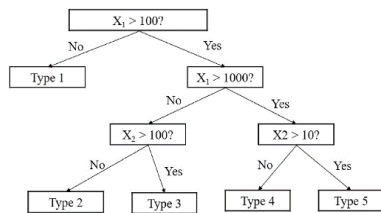


Figure 1 Flow chart of DT (Taken from Huaxing gao, Lang jin et al.)

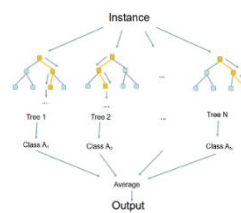


Figure 2 Flow chart of RF (Taken from Huaxing gao, Lang jin et al)

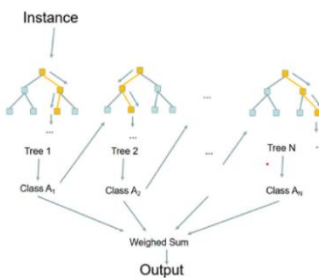


Figure 3 Flow chart of XGBoost (Taken from Huaxing gao, Lang jin et al)

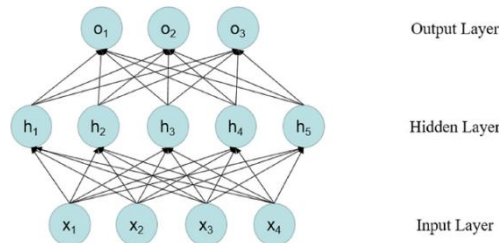


Figure 4 Flow chart of ANN (Taken from Huaxing gao, Lang jin et al)

2.5 ML Applications in 3D Concrete Printing

(Geng et al., 2024) developed a two-stage ML framework: a **Random Forest model** predicted rheological parameters (PV, SYS, DYS), and a second model used these to predict **printability metrics** such as **height error (HE)** and **width error (WE)**. Their results showed $R^2 > 0.90$ for PV and $R^2 = 0.84\text{--}0.99$ across other metrics.(T. Chen & Guestrin, 2016)

Silva et al. (2024) applied **Extreme Gradient Boosting (XGB)** with **computer vision** in a real-time control system. A depth camera (Intel RealSense L515) monitored layer morphology during printing, and the XGB model autonomously adjusted robot motion speed to maintain the desired layer width. A synthetic dataset generated using

OpenFOAM simulations ensured reliable training without extensive physical trials. To specifically simulate the rheological performance of the concrete mixture, the generalized Newtonian fluid (GNF) with yield stress is used. The Herschel-Bulkley model is adopted. Models are described as a non-linear relationship between the shear stress and the shear rate above the yield point. This behavior describes by the equation

$$\tau_{ij} = \tau_0 + 2KD_{ij}^n$$

The equation described is similar to the Bingham model with constant viscosity (Newtonian Fluid).(Nguyen et al., 2011; Paolo et al., 2022)

Six models and five equivalent indicators are used in the research paper. The ML models are RF, SVM, XGBoost, LightGBM, CatBoost and NGBBoost. The indicators are R^2 , MAE, MSE, RMSE, SMAPE. The XGBoost, LightGBM, and Catboost show the R^2 value of 0.99.(Uddin et al., 2023)

$$R^2 = 1 - \frac{\sum_{i=1}^m (y_i - y_i^*)^2}{\sum_{i=1}^m (y_i - \bar{y})^2}$$

$$MAE = \left(\frac{1}{N}\right) \times \sum_{i=1}^N |y_i - \hat{y}_i|$$

$$RMSE = \sqrt{\left(\frac{1}{N}\right) \times \sum_{i=1}^N (y_i - \hat{y}_i)^2}$$

$$RSE = \frac{\sum_{i=1}^N (y_i - \hat{y}_i)^2}{\sum_{i=1}^N (y_i - \bar{y})^2}$$

$$SMAPE = \frac{1}{m} \sum_{i=1}^m \frac{|y_i - y_i^*|}{\frac{|y_i + y_i^*|}{2}} \times 100$$

These applications demonstrate ML's growing role in **closed-loop control**, enabling not just prediction but **active decision-making and adaptation** during printing.

2.6 Explainable Artificial Intelligence (XAI) in Concrete Modelling

To build trust in AI predictions, **Explainable AI (XAI)** methods like SHAP (Shapley Additive Explanations), PDP (Partial Dependence Plot), and ALE (Accumulated Local Effects) are employed.

In (Ghasemi & Naser, 2023) study:

- **SHAP analysis** ranked feature importance: age > fine aggregate > silica fume > cement.
- **PDPs** illustrated how individual inputs affect strength independently.
- **ALE plots**, correcting for feature interaction, showed:
 - Cement (600–700 kg/m³) → +4 to +7 MPa

- Water ($<100 \text{ kg/m}^3$) $\rightarrow +7.5 \text{ MPa}$
- Silica fume ($>70 \text{ kg/m}^3$) $\rightarrow +12.5 \text{ MPa}$

(Uddin et al., 2023) used SHAP to analyze feature contributions in **fiber-reinforced 3DPC**. Water/binder ratio and cement were most influential for compressive strength, while fiber volume was critical for flexural strength.

2.7 Properties of 3D Concrete Printing

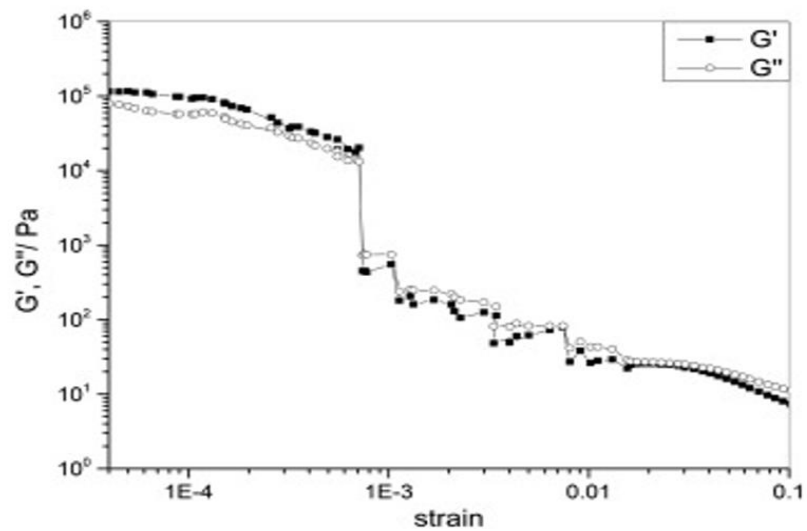


Figure 5 Strain Sweep Analysis of Cement Paste: Results from Qian and Kawashima (2016)

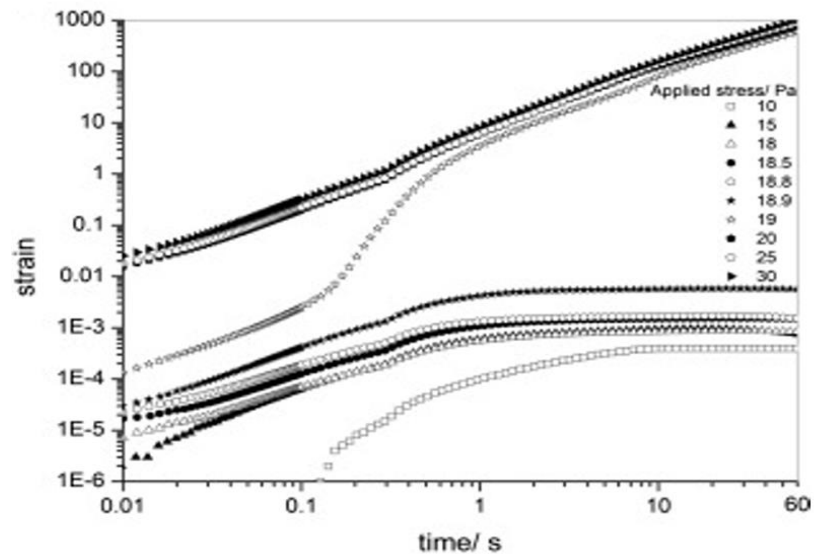


Figure 6 Creep Behavior of Cement Paste at Varying Stress Levels: A Study from Qian and Kawashima (2016)

In oscillatory shear tests, when a strain sweep is performed, the apparent storage modulus of the material declines significantly once the strain amplitude exceeds a critical limit. At the same time, the loss modulus of the paste increases from a relatively low value, eventually surpassing the storage modulus when the strain exceeds this threshold Kawashima et al.,

In the study of Giridhar et al., 2023, total trials were done on the 24 mixes. The study proposed the development of 3D printable concrete mix for the plain and fibre reinforcement. The suggested flow value of the mix that is to be extrudable, printable, and buildable is 190mm to 210mm. and the suggested open time is 2700 sec -3600sec. The results found that the specimens failed monolithically under a single prevailing crack. The elements used are cement, Silica Fumes, Fly ash and limestone. The study identified that the superplasticizer doses ranges from the 0 to 1.5 percent by weight of cement can increase the flowability. Also, the silica fumes dosage from 0 to 10 percent increase can lead to a decrease in the flowability and make the mix non-extrudable. The study identified that the replacement of cement with limestone can lead to shape retention. The optimum speed used is the 3600mm/min. The effects of printing speed is also described in the details. With decrease in printing speed, it not able to extrudable and makes the material stiff inside the nozzle. Whereas an increase in speed leads to the collapse of the layer-by-layer structures.

A flow table test is utilized in this study to create the 3D printable mix. However, the microstructural characterization has not been addressed and will be discussed in future reports. The printed beams exhibited a monolithic failure and demonstrated strong interlayer adhesion during the flexural test. Strain measurements obtained at the tension plane, compression plane, and around the neutral axis were found to be comparable for both printed and control beams. The testing revealed that the printed beams experienced brittle failure, a drawback currently being

addressed, and future publications will present 3D printed beams with strain hardening characteristics.

2.8 Investigating the Rheological and Thixotropic Properties of Cement Paste

Cement paste is classified as a non-Newtonian fluid that shows characteristics of yield stress. When a constant stress is applied below a critical threshold, the deformation of the cement paste slowly stabilizes. However, if the stress surpasses this threshold, the material undergoes continuous deformation at a steady rate over time (Kawashima et al., 2013; Schultz & Struble, 1993). Nehdi and Rahman (2004) identified similar patterns during their stress-sweep experiments in oscillatory shear. In steady-shear tests, the stress response of cement paste eventually becomes stable. When the steady-state shear stress is plotted against the shear rate, the line intersects at a non-zero value when the shear rate is zero, indicating the yield stress of the material. This yield stress can be determined from where the steady-state shear stress curve meets the shear rate (Fernández-Altabe & Casanova, 2006; Hwang et al., 2009; Nessim & Wajda, 2015; Papo, 1988). Furthermore, the slope of the steady-state shear stress versus shear rate curve is not uniform; it diminishes as the shear rate increases, indicating that cement paste exhibits shear-thinning behavior (Papo, 1988). Cement paste also shows thixotropic properties. Under conditions of constant shear rate, the material initially overshoots to a peak value before settling into a steady state. The extent of this overshoot is influenced by the length of the rest period prior to testing, while the constant shear stress remains mostly unchanged by the rest duration (Roussel, 2005).

Cement paste exhibits thixotropic characteristics. When subjected to constant shear rates, the stress first spikes to a peak level before stabilizing at a steady state. The extent of this initial spike is influenced by the length of the rest period before testing, while the steady shear stress remains

largely unchanged by the duration of rest (Roussel, 2005). This initial stress overshoot, which is dependent on the material's prior conditions, is a significant aspect of thixotropic behavior. Additionally, during experiments that involve increasing and decreasing shear, the area within the stress versus shear rate loop progressively shrinks with each cycle, further emphasizing the thixotropic nature of the cement paste (Fernández-Altable & Casanova, 2006; Papo, 1988).

2.9 Identified Research Gaps

Despite progress, significant gaps remain:

- 1.Lack of standardized datasets: Most ML models are trained on heterogeneous or small-scale data, hindering generalization.
- 2.Testing inconsistency: Variation in printability tests (slump, flow, rheology) leads to conflicting benchmarks.
- 3.Environment exclusion: Few models consider ambient temperature, humidity, or printing delays, which impact performance in real-world scenarios.
- 4.Limited real-time integration: Although promising, real-time ML control systems (e.g., Silva et al.) are rare and lack multi-objective optimization.
- 5.Neglect of sustainability metrics: Factors such as CO₂ footprint, energy efficiency, and material circularity are absent from most mix design models, though they are critical for future construction practices.

Chapter 3

Methodology

3.1 AI and ML Models used in predicting mix designs

Where M denotes the feeble learner, the self-dependent tree structure is $f_m(x_i)$, and the weak learners hypothesis space denotes I . XGBoost follows the objectives in the equation below, which is minimized to identify the set of functions applied in the model.

Cement paste is classified as a non-Newtonian fluid that exhibits yield stress properties. When subjected to a consistent stress history that remains below a specific threshold, the deformation of cement paste eventually stabilizes. However, if the stress exceeds this critical level, the material undergoes continuous deformation over time at a fairly steady rate (Struble & Schultz, 1993). In experiments involving a strain sweep in oscillatory shear, it can be seen that the apparent storage modulus of the material significantly decreases once the strain amplitude surpasses a certain critical point. Additionally, the apparent loss modulus can rise from a relatively low value to exceeding the storage modulus at strain levels beyond this threshold (Struble & Schultz, 1993). Similar findings were noted by Nehdi and Rahman (2004) in their stress-sweep experiments in oscillatory shear.

3.1.1 XGBoost

XGBoost has proven effective in addressing highly nonlinear problems, particularly due to its ability to mitigate overfitting through the careful tuning of hyperparameters and its effective handling of missing data. (T. Chen & Guestrin, 2016; Kavzoglu & Teke, 2022) As a gradient boosting decision tree (GBDT) method, XGBoost builds upon the principles of gradient boosting (Bakouregui et al., 2021).

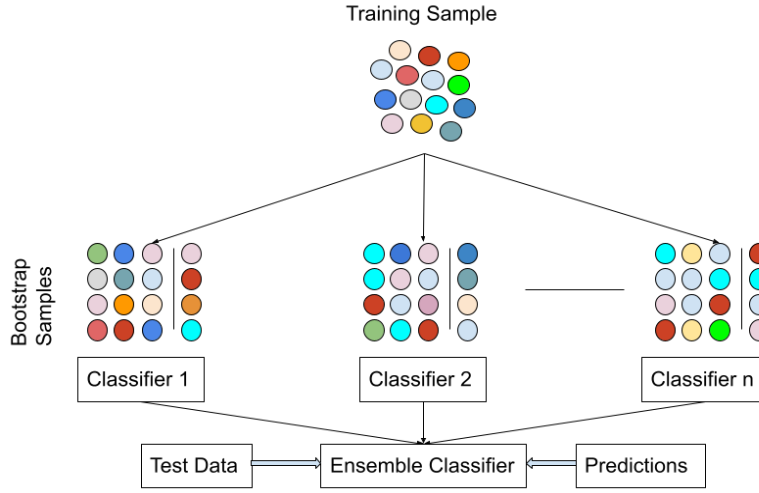


Figure 7 Illustration of the XGBoost Model

Its objective is to reduce the discrepancies between observed and predicted standards by iteratively assembling new decision trees that aim to fit the residuals from prior predictions (Hengl et al., 2017; D. Zhang et al., 2018). Consider a dataset A containing P samples, each with q features, represented as a vector a_i as follows:

$$A = \{a_i, b_i\} (|A| = P, a_i \in R^q, b_i \in R)$$

The output of this model represents $\bar{b}_i = \varphi(a_i) = \sum_{m=1}^M k_m(a_i), k_m \in I$

$$loss(\varphi) = \sum_i f(\bar{b}_i, b_i) + \sum_m \Omega(k_m) \quad (1)$$

The loss function can be shown by $f(\bar{b}_i, b_i)$. Ω is the second regression tree function. (Gao et al., 2024) Overfitting is done to extended regularization terms. The regulation function is expressed in below equation,

$$\Omega(k) = \gamma N + \frac{1}{2} \lambda ||Z||^2$$

Where N is the number of leaf nodes.

γ & λ is the penalty coefficient

z Is the leaf marks (weight).

The prediction for the i th instance during repetition is denoted as \bar{b}_i . To enhance model performance, the term K_r is incorporated into the model, as outlined in Equation (1). To expedite the optimization process, a Taylor expansion is applied to the objective function in Equation (3).

$$loss^t = \sum_{i=1}^p \left(f(b_i, \bar{b}_i^{t-1}) + k_i(a_i) \right) + \Omega(k_i)$$

$$loss^t = \sum_{i=1}^p \left(f(b_i, \bar{b}_i^{t-1}) + k_i(a_i) \right) + \frac{1}{2} m_i k_i^2(a_i) + \Omega(k_i)$$

3

Whereas the first and second loss functions are expressed as

$n_i = \delta_{b_{i_{t-1}}} f(b_i, \bar{b}_i^{t-1})$ and $m_i = \delta_{\bar{b}_i^{t-1}} f(b_i, \bar{b}_i^{t-1})$ respectively. After defining $K_j = \{i | l(a_i) = j\}$ as the instance set of a leaf j . The regularization term Ω can be written as:

$$loss_{split} = \frac{1}{2} \left[\frac{(\sum_{i \in K_a} n_i)^2}{\sum_{i \in K_a} m_i + \lambda} + \frac{(\sum_{i \in K_b} n_i)^2}{\sum_{i \in K_b} m_i + \lambda} - \frac{(\sum_{i \in K} n_i)^2}{\sum_{i \in K} m_i + \lambda} \right]$$

$$\widetilde{loss}^t \cong \sum_{i=1}^P \left[n_i k_t(a_i) + \frac{1}{2} m_i k_t^2(a_i) \right] + \gamma N + \frac{1}{2} \lambda \sum_{j=1}^N z_j^2$$

The optimal weight z_j^α of the leaf j is represented as:

$$z_j^\alpha = - \left(\frac{\sum_{i \in K_j} n_i}{\sum_{i \in K_j} m_i + \lambda} \right)$$

The objective function can be calculated in equation 4

$$\widetilde{loss}^t(l) = -\frac{1}{2} \sum_{j=1}^N \frac{(\sum_{i \in K_j} n_i)}{\sum_{i \in K_j} m_i + \lambda} + \gamma N \quad \dots\dots 4$$

To evaluate the quality of a decision tree split, the scoring function III is employed. The sets K_a and K_b represent the instances allocated to the left and right child nodes, respectively, following the split. The reduction in impurity or damage as a result of this split is quantified using Equation (5).

3.1.2 Support Vector Machine

Support Vector Machines (SVM) are vigorous supervised learning algorithms commonly applied in both classification and regression tasks. The main aim of a Support Vector Machine (SVM) is to find the best possible line or surface that can clearly separate two different groups in a high-dimensional space. It's like drawing a boundary that helps us tell one class from another. This process typically involves several stages: importing necessary libraries, pre-processing the data, applying feature scaling, choosing an appropriate kernel function, training the model, tuning hyper parameters, and assessing the model's performance (Zhou et al., 2017).

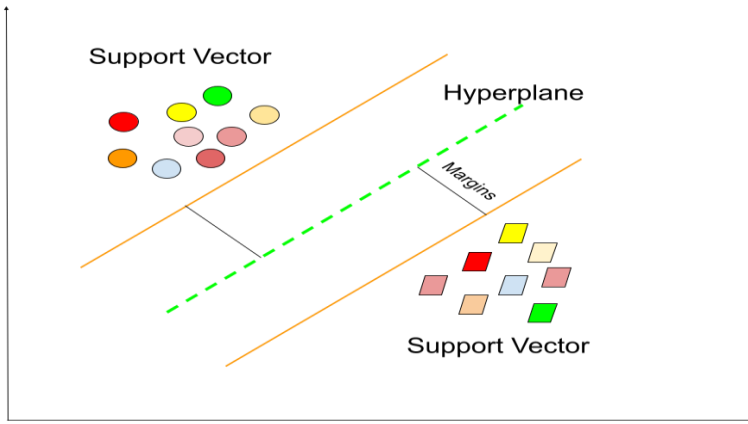


Figure 8 Illustration of the Support Vector Machine Model

SVMs have the capability to confront complex classification problems by utilizing kernel functions, which let the algorithm to operate in a lower-dimensional space while solving problems that are inherently high-

dimensional and non-linear. Selecting the right kernel function is critical, as it directly influences the precision and effectiveness of the model (Agrawal & Chakraborty, 2021; Laref et al., 2019). An unsuitable kernel can lead to poor predictive performance (Ayat et al., 2005). For a given dataset with n samples, the linear model used in SVM can be represented in the function space $f(a, w)$, as described in Equation (5)

$$f(a, w) = \sum_{i=1}^n w_i z_i(a) + p \quad (5)$$

Where $z_i(a)$ represents a set of nonlinear mappings, and the associated weight vector in n -dimensional space is denoted by w , while p refers to the bias term. Therefore, the support vector regression (SVR) approach aims to minimize an objective function, denoted as l_ϵ (Eq. (6)) (Chou et al., 2014), (Chou et al., 2014). The primary aim is to reduce empirical error by identifying the most suitable value for the weight vector w .

$$l_\epsilon = l_\epsilon(b, f(a, w)) = \begin{cases} 0 & \text{if } |b - f(a, w)| \leq \epsilon \\ |b - f(a, w)| & \text{otherwise} \end{cases} \quad (6)$$

A key advantage of the kernel method in support vector machines (SVM) is its ability to manage high-dimensional data while keeping the model relatively simple. This is achieved by minimizing $\|w\|^2$ a fundamental feature of the SVM kernel trick (Ayat et al., 2005; Chou et al., 2014; Laref et al., 2019). In this context, slack variables are introduced and represented by λ_i , and λ_i^* . This approach is derived from Vapnik's theory of ϵ -insensitivity. The SVR model is mathematically detailed in Equation (7).

$$\begin{aligned} & \text{minimize } \frac{1}{2} \|w\|^2 \\ & + C \sum_{i=1}^n (\lambda_i, \lambda_i^*) \text{ subject to } \begin{cases} b_i - f(a_i, w) \leq \lambda_i + \epsilon \\ f(a_i, w) + b_i \leq \lambda_i^* + \epsilon \\ \lambda_i, \lambda_i^* \geq 0, i = 1, 2, 3, \dots, n \end{cases} \end{aligned}$$

$$f(a) = \sum_{i=1}^{n_{svm}} (\beta_i - \beta_i^*) k(a, a_i) \text{ Subject to } 0 \leq \beta_i \leq C, 0 \leq \beta_i^* \leq C$$

Where the number of supports vector is n_{svm} . Equation 9 represent the kernel function. The kernel function is used to determine the support vector.

$$k(a, a_i) = \sum_{i=1}^m z_i(a) z_i(a_i)$$

3.1.3 Random Forest

Random Forest (RF) is a commonly adopted technique within the machine learning domain, recognized as a powerful ensemble-based method. It is particularly known for handling complex and high-dimensional datasets while still delivering reliable performance in terms of accuracy and model generalization. This method is especially beneficial in evaluating various properties, including those in composite and recycled construction materials (Li et al., 2022; Yuan et al., 2022). The RF approach builds upon the decision tree architecture by combining multiple trees, each trained on different portions of the dataset and selected features (Zhang et al., 2018). Its adaptability has led to widespread use across multiple domains such as finance, healthcare, biological research, and image analysis. It plays a significant role in areas like anomaly detection, disease prediction, gene pattern identification, and image classification.

In classification problems, RF's performance is commonly measured using evaluation criteria such as accuracy, precision, recall, and the F1 score. For regression models, it employs measures like mean squared error (MSE), mean absolute error (MAE), and the coefficient of determination (R^2). Additionally, techniques like k-fold cross-validation can be employed to gauge the model's performance on unseen data.

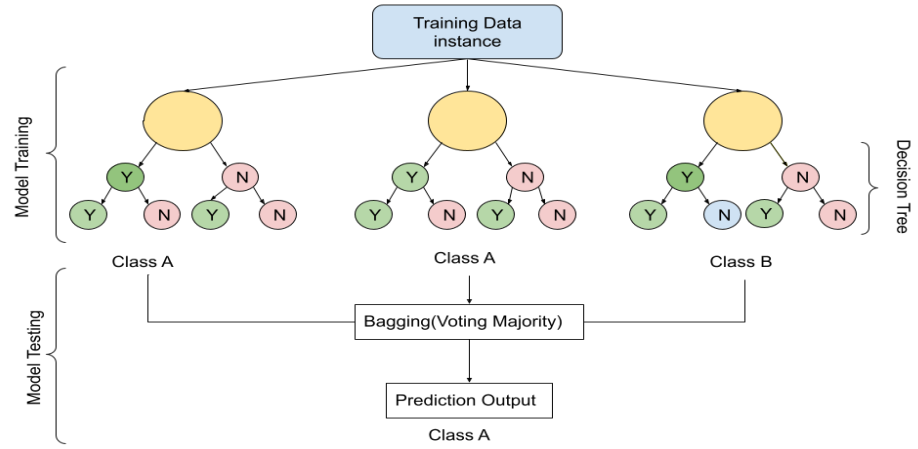


Figure 9 Illustration of the Random Forest

Adjusting hyperparameters plays a critical role in boosting the performance of Random Forest (RF) models. Techniques such as manual adjustment, grid-based exploration, random search, and Bayesian approaches are commonly used to enhance predictive precision and improve generalization on unseen datasets. Additionally, scholars have utilized metaheuristic methods to fine-tune hyperparameters, thereby increasing the stability and robustness of predictive models (du Plessis et al., 2021). The dataset used for training, denoted by M_n and comprising n instances, is structured as follows:

$$M_n = \{(x_1, y_1), (x_2, y_2), (x_3, y_3), \dots, (x_n, y_n)\} (x_i \in M_1, y_i \in M)$$

Here, n refers to the total number of samples in the training set. The overarching function, denoted as $y = a(x, M_n)$, is determined based on the training dataset M_n and involves several steps, including data preparation and tuning of hyperparameters. Subsequently, the ensemble of decision trees yields a result based on the average of their individual outputs.

$$(i.e., \bar{Y}_1 = \bar{a}(x, \bar{M}_1), \bar{Y}_2 = \bar{a}(x, \bar{M}_1), \bar{Y}_3 = \bar{a}(x, \bar{M}_1) \dots \bar{Y}_t = \bar{a}(x, \bar{M}_t).$$

The final output observed as a function in built-in equation below as a new input vector x :

$$y = \frac{1}{k} \sum_{n=1}^1 \bar{y}_n = \frac{1}{k} \sum_{n=1}^k \bar{a}(x, \bar{M}_n)$$

The final evaluation assesses the strengths and weaknesses of the model, offering suggestions for further enhancements or applications.

3.1.4 Decision Tree

A DT is a machine learning algorithm that makes decisions by breaking down the data into smaller, more manageable parts based on the specific conditions. It repeatedly splits data based on features until it reaches a conclusion. (Gao et al., 2024) Decision Trees are easy to understand and visualize, making them a straightforward yet powerful tool for machine learning tasks. However, they can over fit the data without proper management by becoming overly complex. To prevent this, techniques like pruning or limiting the tree's depth are often employed. (Ghasemi & Naser, 2023)

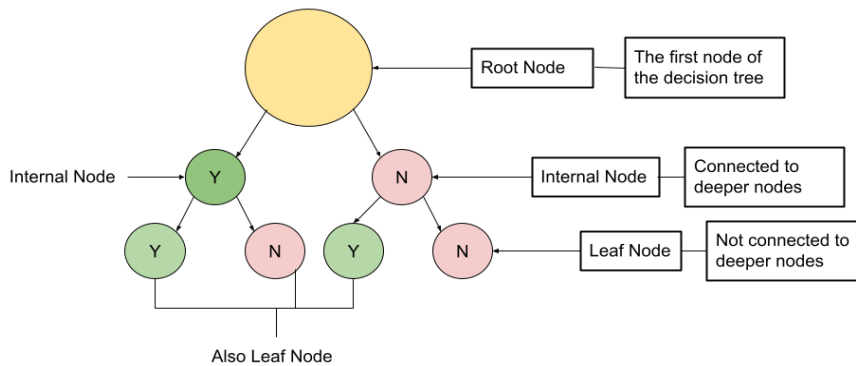


Figure 10 Illustration of the Decision Tree

3.1.5 Artificial Neural Network (ANN):

During the 1940s, the concept of artificial neural networks (ANNs) emerged, inspired by the structure and functioning of the human brain and nervous system. Unlike conventional computing systems, the human brain excels at adaptive learning and problem-solving, despite operating at slower speeds (Ren et al., 2019). ANNs are designed to replicate some of these cognitive abilities by leveraging data from past experiences to make informed decisions. Among the various learning techniques used in ANNs, feed-forward backpropagation (FFBP) stands out as one of the most widely applied methods (Z. Li et al., 2017). Its popularity in earlier research stems from its simplicity and strong predictive capabilities (Agrawal & Chakraborty, 2021).

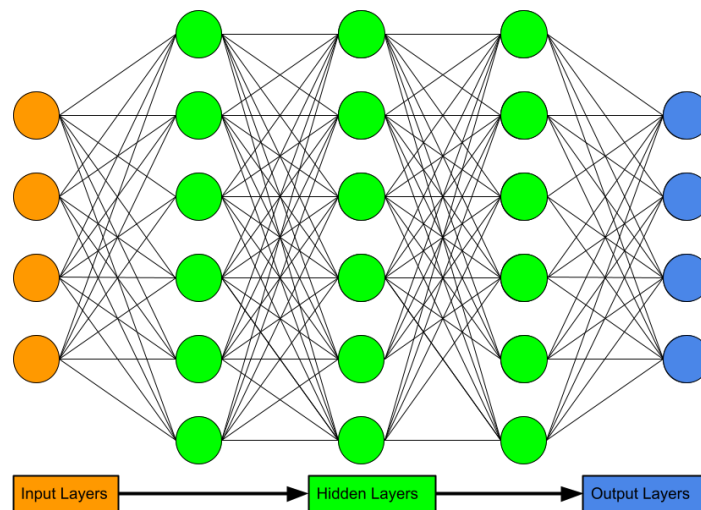


Figure 11 Illustration of ANN

An FFBP network typically consists of multiple layers, each composed of a specific number of neurons. The architecture begins with an *input layer*,

which receives raw data and passes processed signals through to subsequent layers. The last layer, known as the output layer, produces the network's predictions or decisions. The number of neurons in the input and output layers usually corresponds to the number of input features and desired outputs, respectively. Between these layers, there may be one or more *hidden layers* responsible for the network's internal computation. Each neuron in a given layer is fully connected to every neuron in the adjacent layer via weighted links. The overall accuracy of the ANN is influenced by the number of neurons and hidden layers used; however, increasing the network's complexity often leads to higher computational demands as well as improved performance (Z. Li et al., 2017; Ren et al., 2019)(Laref et al., 2019). Figure 11 presents a schematic of a multi-layer ANN including a hidden layer.

3.2 AI and ML Models used in predicting mix designs

This study demonstrate the uses of ML models in 3D concrete printing. Total 100 research papers were collected and reviewed.(Chaves Figueiredo et al., 2019; Y. Chen, Chaves Figueiredo, et al., 2020; Y. Chen, Romero Rodriguez, et al., 2020; Ding, Xiao, Zou, & Wang, 2020; IZADGOUSHI et al., 2021; Ma et al., 2018, 2019; Panda et al., 2019)(Khalil et al., 2017; Le et al., 2012; Liu et al., 2022b, 2022a; Marchment et al., 2019; Mechtcherine et al., 2019; Pham et al., 2020; J. Xu et al., 2019; Y. Zhang et al., 2019)(Huang et al., 2018; Panda & Tan, 2019; Papachristoforou et al., 2018; Perrot et al., 2016; Van Der Putten et al., 2019; Wang et al., 2020; Xiao et al., 2020; Y. Xu et al., 2021; Zareiyan & Khoshnevis, 2017) (Albar et al., 2020; M. Chen, Li, et al., 2018; Y. Chen, He, et al., 2021; Chu et al., 2021; Cicione et al., 2021; Heras Murcia et al., 2020; Moeini et al., 2020; Tarhan & Şahin, 2021a)(Baz et al., 2020; M. Chen, Guo, et al., 2018; H. Li et al., 2017; Long et al., 2019; Manikandan et al., 2020; Markin et al., 2021; Rahul et al., 2022; Suntharalingam et al., n.d.; Y. Xu et al., 2020)(Bong et al.,

2021; M. Chen, Li, et al., 2020; M. Chen, Yang, et al., 2020; Y. Chen, Zhang, et al., 2021; Ding, Xiao, Zou, & Zhou, 2020; Kim et al., 2018; Kruger et al., 2020; Nerella et al., 2019; Sun et al., 2020) and more. To access the papers, [click here](#). From that 100 previous published research papers approximately 500 data points were gathered. The complete database is available on the cloud drive.

3.3 Data Collection and Analysis

Collected more than 500 printable mix designs from the latest published Out of the total 500 mix designs of 3DCP. This data is compiled from the 100 relevant research paper of 3DCP, It highlights the broad spectrum of relevant research happening around the world, showcasing a variety of

Out of the total 500 mix designs of 3DCP. This data is compiled from the 100 relevant research paper of 3DCP, It highlights the broad spectrum of relevant research happening around the world, showcasing a variety of

On the basis of the resulting predicted mix designs the few designs are being tested which shown as above. The mortar resembles the properties of 3D

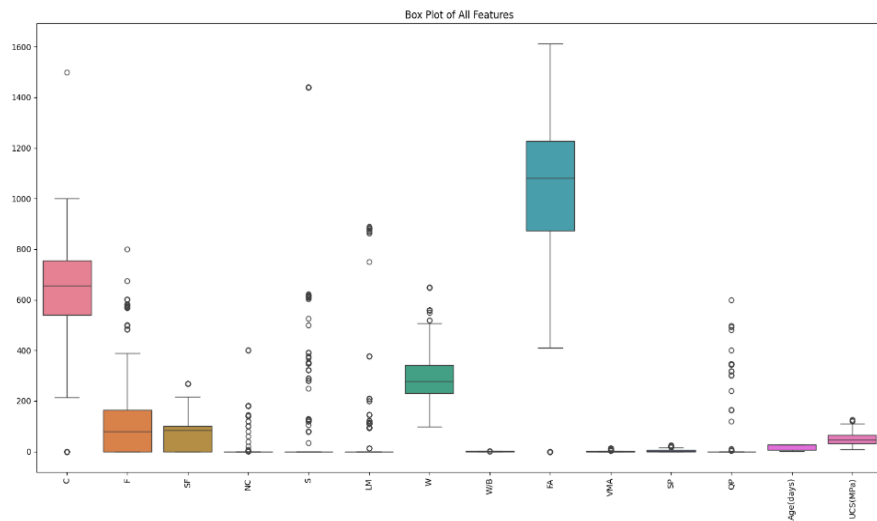


Figure 12 Variation of Mix Design Components in 3D Printable concrete



Figure 13 Scatter Plot Diagram of Mix design for 10 input variables.

concrete mix designs and the tests used to assess their properties. The data has been collected, cleaned, arranged, and formatted as per requirements. After cleaning and formatting the data, total 10 input variables are considered; those are cement (C, kg/m³), Fly Ash (FA, kg/m³), Silica Fumes (SF, kg/m³), Nano-Clay (NC, kg/m³), Sand, (S, kg/m³), Limestone (LM, kg/m³), Water (W, kg/m³), Fine Aggregate (FA, kg/m³), VMA (VMA, kg/m³), Super-plasticizer (SP, kg/m³). The loading condition considered in Y direction only. In this project, 400 values have been training to predict the compression test of 3D concrete printed samples. The box plot diagram shows the range of material weights in the mix design that is used to cast the models.

3.4 Materials and Methods

For the current study, OPC-43, (IS 8112:2013), fly ash conforming to Class F-ASTM, and a silica fumes is used as binders. The specific gravities are 3.15, 2.6 and 2.2, respectively. The chemical admixtures used are super-plasticizer, Admixtures and thickener agent. The size of sand used are under

600 μ . The size of clay particles used are 1.5-2 μ . The specific gravity of sand are 2.64.

printed concrete. The casted samples are printed from a 3DCP which has the above constituents. The box plot visualizes the distribution of several features, including C, F, SF, NC, S, LH, W, WIB, FA, WMA, SP, GP, Age (days), and UCS (MPa). Features like **C** and **F** exhibit a wide distribution with significant variability and several outliers, while **SF** and **NC** show narrower, more concentrated distributions. **W** and **WMA** have compact distributions with fewer extreme values. **Age (days)** and **UCS (MPa)** also have concentrated distributions, with **Age** having notable outliers. The plot highlights data variability, the central tendency and the presence of outliers, which may require further investigation in the analysis or modelling stages

3.5 Correlation Matric

Ensemble techniques in machine learning involve combining several models, often simpler ones, to form a stronger and more accurate predictive model. These strategies help boost accuracy and lower the chances of overfitting.

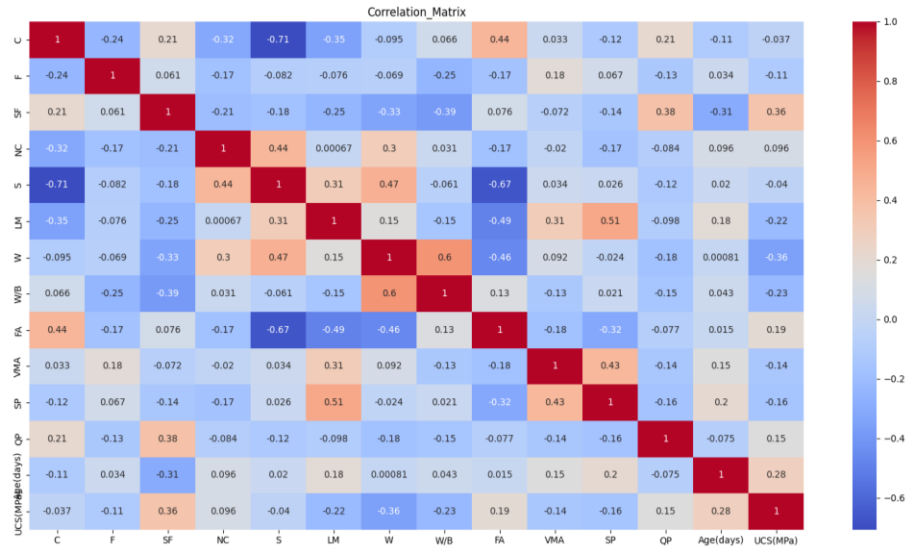


Figure 14 Correlation Matrix

Overfitting happens when a model does a great job with the training data but fails to do the same with new data it hasn't seen before. The correlation matrix highlights their linear relationships. Strong negative correlations are observed between **C** (cement content) and **S** (strength) (-0.71), suggesting that increasing cement content may reduce strength, and between **C** and **FA** (fine aggregates) (-0.44), implying a trade-off between these two features. Strong positive correlations are found between **W** (weight) and **W/B** (water-to-binder ratio) (0.6), as well as between **SP** (slump) and **FA** (0.51), indicating that higher fine aggregate content and water-to-binder ratios enhance workability. Moderate positive correlations, such as between **Age** (days) and **UCS** (MPa) (0.28), show that material strength increases with age. Weaker or negligible correlations, like between **LM** (limestone content) and other features, suggest that some variables have little impact on others. This correlation matrix provides valuable insights for feature selection in

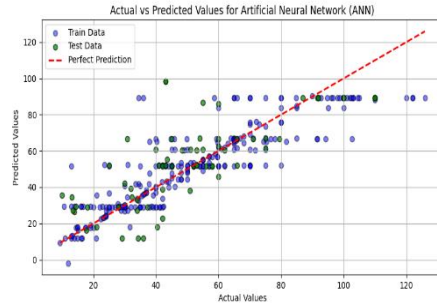


Figure 15 Comparison of ML Model(ANN)

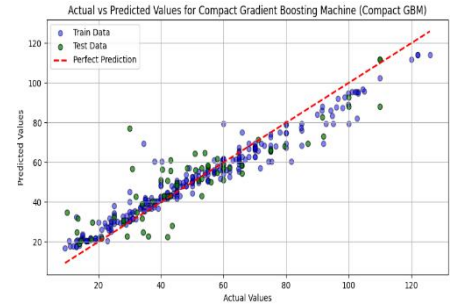


Figure 16 Comparison of ML Models(GBM)

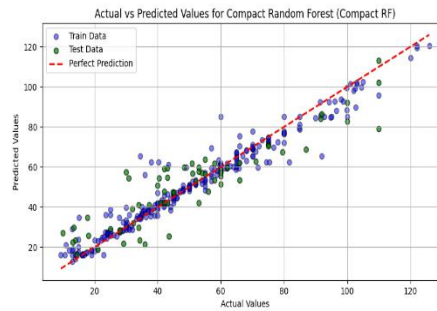


Figure 18 Comparison of ML Model performance-Compact RF

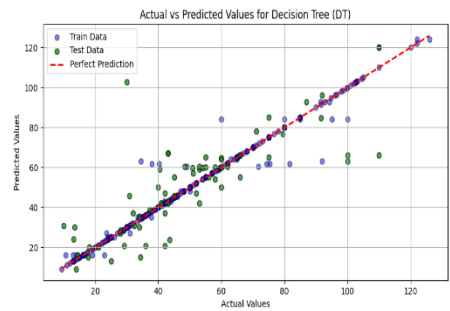


Figure 1 Comparison of ML Model performance- DT

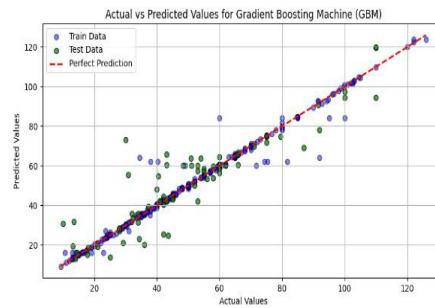


Figure 20 Comparison of ML Model performance - GBM

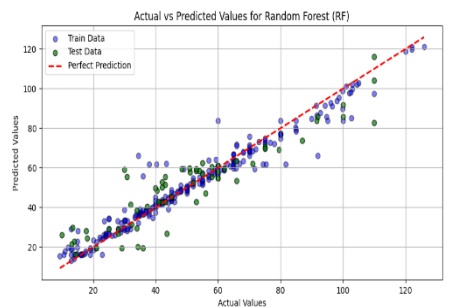


Figure 20 Comparison of ML Model performance- RF

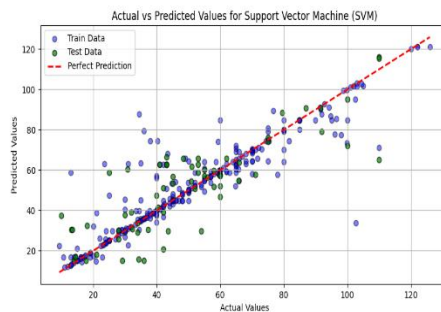


Figure 21 Comparison of ML Model performance- SVM

Modelling, optimizing material compositions, and understanding the relationships between different material characteristics.

3.6 Prediction and Evaluation of ML Model Performance

Table: 1

Materials	mean	Std. Division	p0	p25	p50	p75	p100
C	632	211.9	0	539	656.6	755.6	1500
F	124.8	161.9	0	0	79.2	165	800
SF	73.43	69.13	0	0	83.78	101.4	268
NC	14.46	54.04	0	0	0	0	400
S	108.6	279.5	0	0	0	0	1440
LM	50.99	164.8	0	0	0	0	888.9
W	295.6	103.9	99	230	277.5	342	648
W/B	0.305 6	0.123	0.103 7	0.22	0.297 5	0.345 7	1.333
FA	971.7	373.3	0	872	1080	1228	1612
VMA	1.133	2.326	0	0	0	1	13
SP	3.66	5.768	0	0	0.446	6.38	26.2
QP	32.99	104.5	0	0	0	0	600
Age(days)	19.92	11.03	1	7	28	28	28
UCS(MPa)	51.21	25.49	9.33	32.12	47	65.9	126
Density	2310	236.6	1163	2152	2301	2444	3581

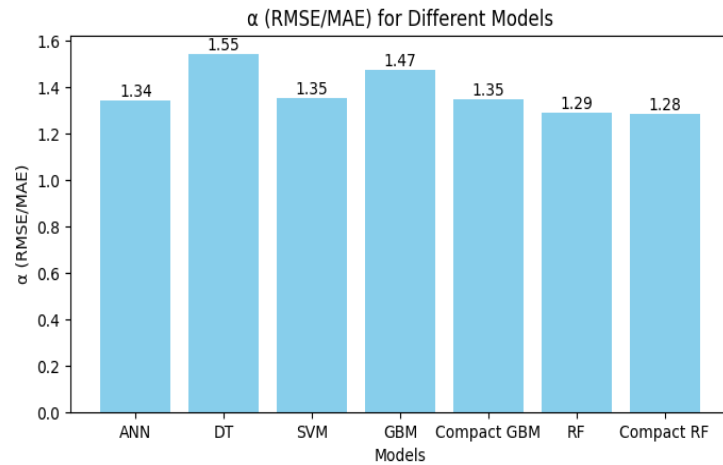


Figure 22 RMSE/MAE Performance value for compressive strenath

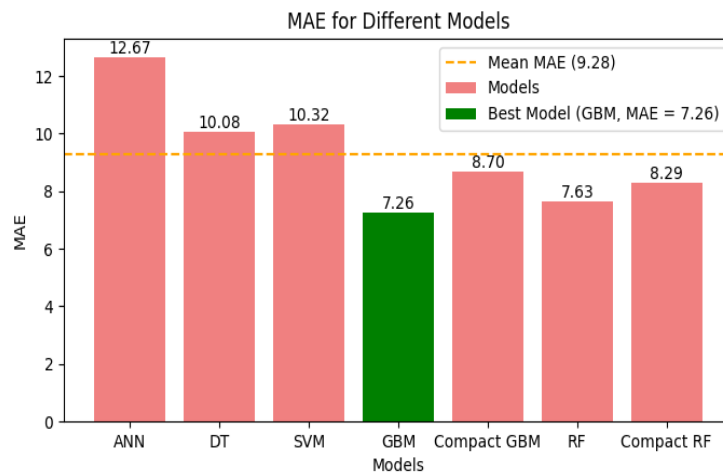


Figure 23 MAE Performance values - Compressive Strenath

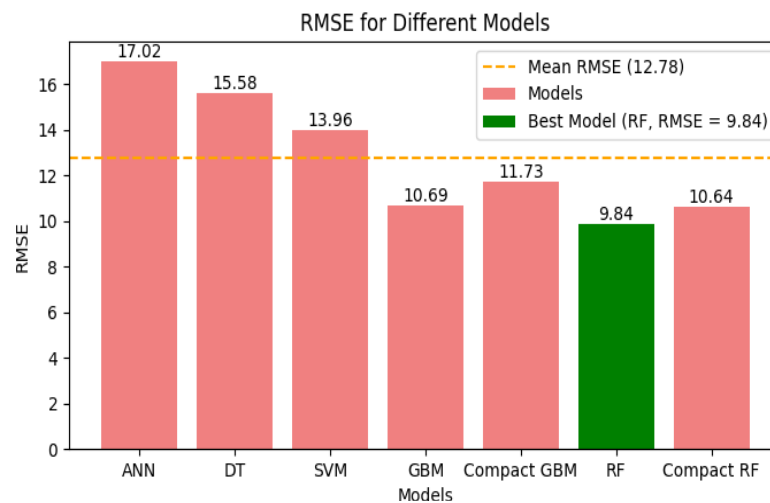


Figure 24 RMSE Performance values - Compressive Strength

3.7 SHAP for Compressive Strength

The image showcases a SHAP summary plot, which highlights how different features affect the model's predictions. Each dot on the plot represents a feature's SHAP value, showing just how much that particular feature is influencing the model's output. The horizontal axis shows the SHAP values, with negative values indicating a decrease in the prediction and positive values suggesting an increase. Features such as **W** (likely weight) and **Age (days)** demonstrate significant impacts, with their higher values leading to stronger positive contributions to the output, as seen by their shift towards higher SHAP values. The color gradient reflects the feature value, with red indicating high values and blue indicating low values. Features like **C** (cement content) and **F** (fine aggregate) show moderate to low impacts, with their contribution varying as their values change. This plot provides valuable insight into which features are most influential.

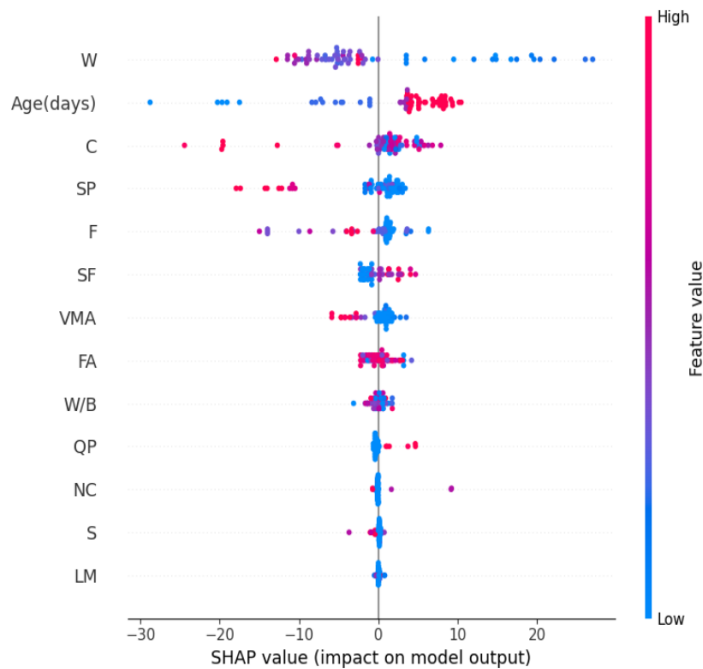


Figure 25 SHAP analysis for the 3D printable mix design

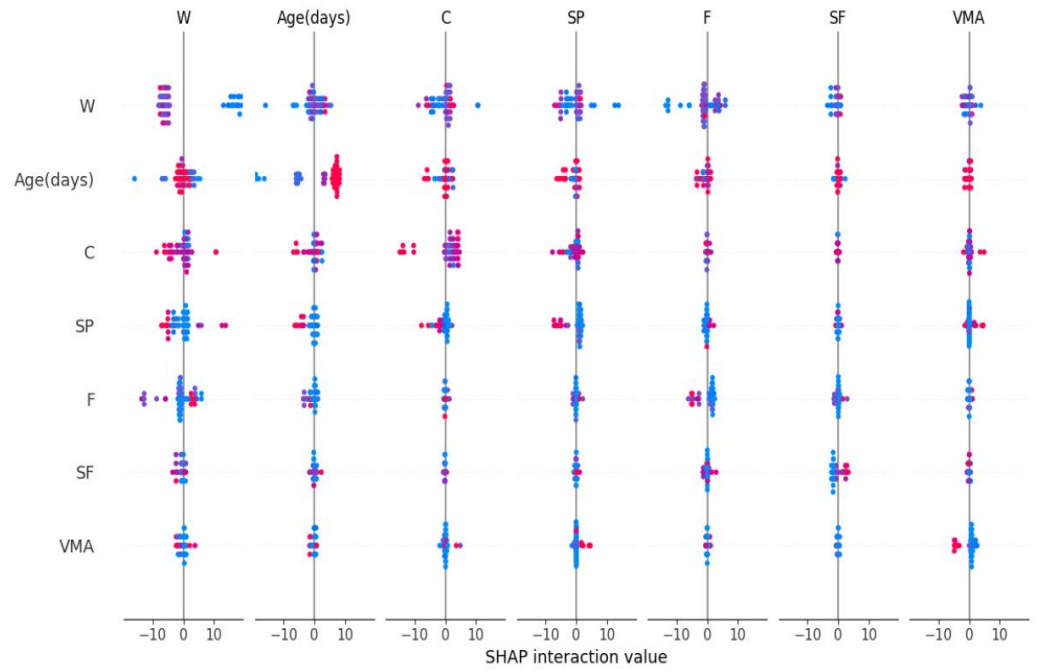


Figure 26 SHAP analysis for the 3D printable mix design

Chapter 4

Experimentation of 3DCP

4.1 General

In chapters 1 and 2, the discussions were made about the introduction and literature review of the three dimensional printed concrete elements. The mix development approach used is the latest available machine learning models and Artificial Intelligence tools. Total 500 data samples were collected from various literature till the today. The all extrudable and buildable mix designs were listed in the excel. Considering a 12 elements including Cement, Fly ash, silica Fumes, Nano clay, blast furnace slag, limestone powder, Sand, VMA, Super plasticizer, Quartz powder, PP Fibers, Steel fibers. The results were listed which came from these data in to the excel those are compressive strength (MPa) for 3 day, compressive strength (MPa) for 7 day, compressive strength (MPa) for 28 day, Flexure strength at 7 days and Flexure strength at 28 days, the workability, consistency, and Flowability.

4.2 3D Printer Platform Calibration

The mixing was done in rotating based machine Kappa PS180VM Universal mixing machine. At a time we have mixed a 100Kg. The water , SP and VMA is prepared with suitable mix proportions. At first the all dry material mixed. It is rotated for at least 10 minutes, so that all the fine materials and particles are mixed homogeneously. Then a liquid mix was added slowly and rotated for 5 minutes at a speed of 300 RPM. The materials were self-flowable and thick, which can be extrudable and buildable.

4.3 Test Bed Printer and Its Calibration

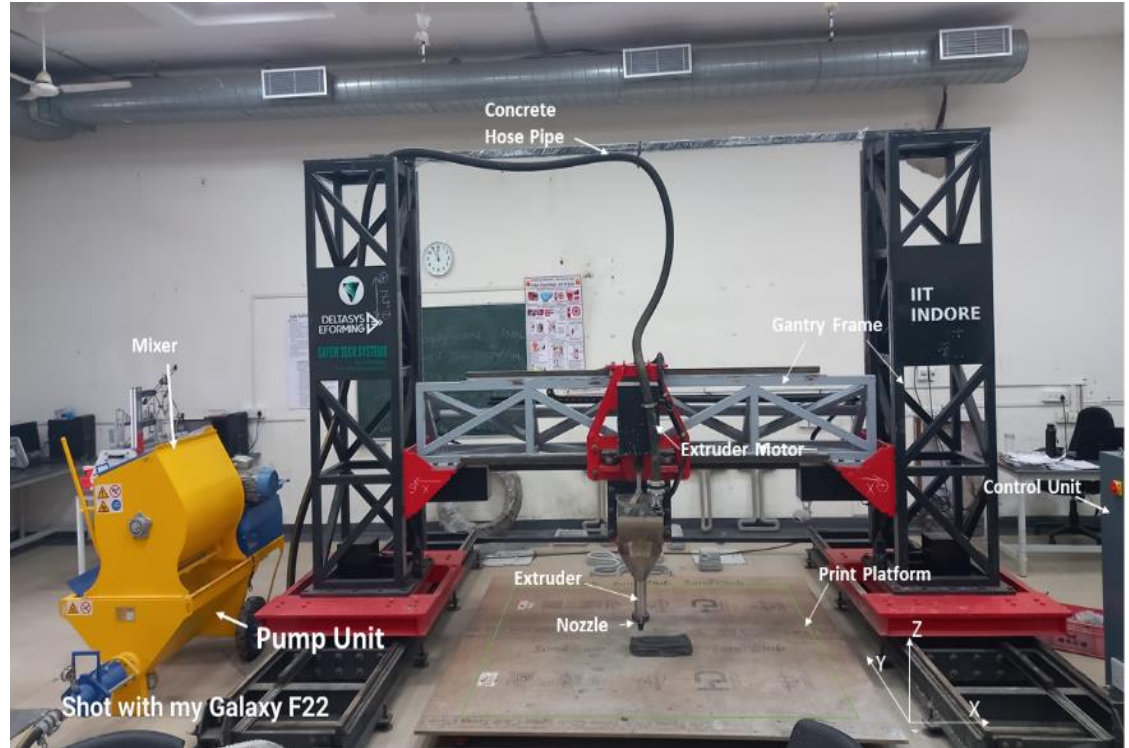


Figure 27 Gantry based 3DCP, POD, IIT Indore

The printing with a large scale 3D printing required an accurate proportioning of materials and calibration of all motors. Printers have total 5 motors. In gantry-based 3D concrete systems, precise and robust motion control is achieved through the industrial-grade motors across primary movement axes. The X-axis is powered by two **stepper motors**, each delivering a holding large torque. These motors are configured in a synchronized dual-drive setup to maintain parallelism and ensure smooth longitudinal motion along the gantry, compensating for the increased mass and potential mechanical deflection in large-format printing. The Y-axis employs a similar configuration with two **closed-loop stepper motors** equipped with **integrated encoders** for real-time position feedback, ensuring high precision and avoiding step loss during extended print cycles. For the extrusion system, a single **AC geared motor** is utilized, enabling it to deliver a continuous torque at low speeds up to 300 rpm rotational speeds.

This torque is necessary to drive a **screw-based extrusion mechanism**, capable of handling high-viscosity concrete mixtures and maintaining a steady material flow through the nozzle, which is critical for achieving consistent layer deposition and structural integrity in printed elements.

4.4 Test Bed

The gantry-based 3D printing system features a printing platform of **2m x 2m** with a maximum print height of **1.5m**, making it suitable for producing large-scale concrete structures such as walls, beams, and architectural features. The system operates on a rigid gantry mechanism that moves along the X, Y, and Z axes, ensuring precise extrusion and layer bonding. It allows for fine control over material deposition, providing high accuracy and stability during the printing process, which is essential for producing complex geometries. The automated system is designed to work with various 3D printable concrete mixes, offering flexibility for customized



Figure 28 Pump integrated material mixer -3DCP. POD, IIT Indore.

designs while maintaining structural integrity. With the capability to scale in size, the system is ideal for both standard construction projects and

innovative, large-scale applications, such as eco-friendly housing or artistic structures, offering versatility and precision with reduced construction time.

4.5 Pump integrated 3D Concrete Mixer

The mixer employed (Fig. 28) in this study possesses the capacity to homogenously blend up to 100 kg of material per batch. Mixing efficiency is ensured by four symmetrically arranged blades within the mixer. Post batching, materials are manually loaded into the mixer, where thorough mixing occurs. Upon completion, the mixed concrete discharges into a collection pan positioned directly beneath the mixer. Subsequently, the material is transported through a flexible hose pipe. Its internal diameter is 60 mm. It is approximately 5m in length. Material flow through this pipe is facilitated by a high-torque, stepper motor-driven pump, providing a consistent volumetric displacement rate. The entire extrusion setup, including the pumping mechanism and the 3D printer itself, is synchronized via an integrated control system. This control system precisely governs the printer's motion trajectory and regulates the extrusion rate at the printing nozzle. Ultimately, the material is extruded through interchangeable nozzles of varying dimensions, depending on specific printing requirements.

If Q represents the pump's discharge rate, V_1 indicates the velocity of the material as it leaves the nozzle (refer to Fig. 29), and cross-sectional area of the nozzle is A_1 , then the discharge Q can be expressed as follows.

$$Q = V_1 \times A_1 \dots \dots \dots A$$

If V_2 represents the speed at which the nozzle travels across the print bed, as illustrated in Fig.29, and A_2 denotes the cross-sectional area of a layer being extruded, then the velocity V_2 can be defined by

$$V_2 = \frac{Q}{A_2} \dots \dots \dots B$$

Substituting from Equation (A) in Equation (B),

$$V_2 = V_1 \times \frac{A_1}{A_2}$$

To maintain its shape, the cross-sectional area of the extruded material will

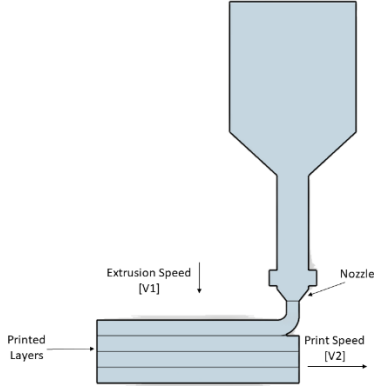


Figure 29 Extrusion Speed (V_1) and Printing speed (V_2)



Figure 30 Extruded layers with uniform thickness and Height

match that of the nozzle size with acceptance of 1mm variation.

Consequently, equation (A) can be simplified to.

$$V_1 = V_2$$

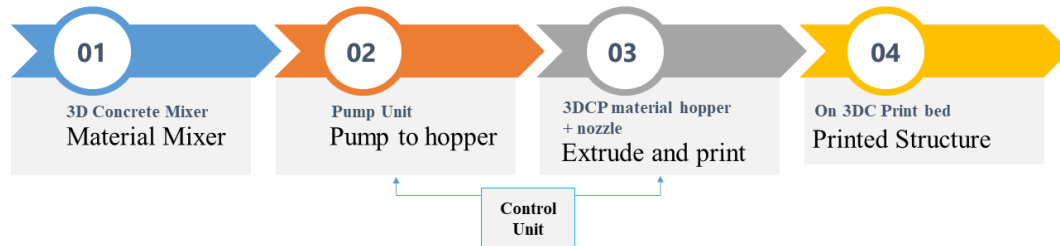


Figure 31 Flow diagram showing the printing process

Consequently, the Concrete printer was adjusted so that the print speed V_1 matched the extrusion speed V_2 . In this research work, all experiments were conducted with extrusion speed of 3600 mm/min. Nonetheless, the formulation and flowability of the mixture also rely on various printing parameters, including the type of pump, extrusion speed, print speed, and the nozzle's shape and size. These factors were not explored in this study.

Chapter 5

Mix proportions, Tests and concrete Printing

5.1 General

Mix trials are done for the mix designed found out from the predicted influential materials from the best ML Model. The influential parameters are SP, VMA, Clay, and Silica Fumes. Thus the proportion of these elements are varies by making the constant other term. All the trials are tested with the extrudability, buildability, and flow table test. Total 14 trails carried out to obtained a printable concrete. The mix proportions are mentioned in table X. The Nomenclature for the sample is for the “3DCPTL01”, is the short form of Three-dimensional concrete printing trail 01. The table demonstrates the behavior of concrete for various trials. It is found that as the VMA decrease from 9.75 to .0975, the mix becomes stiff and changes its properties. The mix becomes non extrudable and stiff.

5.2. Components of 3DCP Mix

5.2.1 Cement

Cement is the primary binder in 3D printable concrete (3DPC), typically made up of compounds such as calcium silicates (C3S, C2S), calcium aluminates, and alumino-silicates. These compounds undergo hydration when mixed with water, forming calcium silicate hydrate (C-S-H), which provides strength and durability to the concrete. The cement content in 3DPC usually ranges between 350–550 kg/m³, which significantly influences the mix’s extrudability and mechanical properties. While higher cement content can increase strength, it may lead to higher shrinkage and cracking, making the mix stiffer and harder to extrude. Conversely, reducing cement content improves workability but may compromise the structural integrity of the printed layers.(Rahul et al., 2019b)

5.2.2 Sand

Sand serves as a fine aggregate in 3D printable concrete, making up about 30%–50% of the total mix. The particle size distribution of sand impacts the material's flowability, extrudability, and stability. Finer sands are preferred for 3DPC, as they provide better extrusion characteristics and improve the shape stability of the printed layers. If the sand content exceeds the optimal range, it may cause the mix to become excessively stiff, reducing extrudability and leading to difficulties in layer deposition. Studies have shown that a sand-to-cement ratio between 1.5 and 2.0 optimizes printability while minimizing material waste during printing.

5.2.3 Fly Ash

Fly ash is a pozzolanic material that is commonly used in 3DPC, typically comprising 15%–30% of the mix. It reacts with calcium hydroxide released during the hydration of cement, forming additional C-S-H, which contributes to long-term strength and durability. Fly ash also helps reduce the heat of hydration, making it especially useful in large-scale 3D printing applications. However, fly ash tends to slow down the setting time, which can increase the open time and allow more time for extrusion. This characteristic is beneficial for printing complex geometries, but excessive use can also make the mix too slow to set, affecting buildability over time.

5.2.4 Silica Fume

To enhance the durability and strength of a 3DCP, Silica fume is added. It is an ultra-fine, amorphous form of silica that is added in small amounts, typically around 3% to 5%. Silica fume reacts with calcium hydroxide during hydration, increasing the density and strength of the material by forming additional C-S-H gel. While it improves layer bonding and interlayer cohesion, excess silica fume can reduce the flowability and extrudability of the mix, making it harder to pump through the extrusion

system. Typically, a silica fume content of 3%–4% achieves the best balance between strength enhancement and workability.

5.2.5 Superplasticizer (SP)

Superplasticizers (SP) are high-range water-reducing agents used to increase the flowability of 3DPC without adding extra water. They disperse cement particles, reducing interparticle friction and allowing the mix to flow more easily. SP is typically used in doses of 0.05%–0.1% by weight of cement.(Mohan et al., 2021) While SP extends open time and improves extrudability, excessive use can reduce the yield stress of the mix, making it harder for the material to retain its shape after extrusion. Balancing the use of SP is critical to avoid compromising the layer stability and interlayer bonding that are essential for maintaining the structural integrity of printed components.

5.2.6 Viscosity Modifying Agents (VMA)

Viscosity Modifying Agents (VMA) are used to adjust the viscosity of 3DPC, enhancing its extrudability and shape stability. VMAs increase the yield stress and viscosity, helping to prevent segregation and slumping of the material after extrusion.(Mohan et al., 2021; Rahul et al., 2022) They are typically added in small amounts (around 0.1%–0.5% by weight). However, excessive use of VMA can lead to increased viscosity, which can impair the material's ability to flow through the nozzle, making it difficult to pump and extrude. Therefore, finding the optimal dosage is essential to ensure the material remains extrudable while maintaining layer stability.

5.2.7 Water

Water is an essential component in the hydration process of cement and is responsible for the workability, strength, and durability of 3DPC. The water-to-cement ratio (w/c) plays a crucial role in determining the final properties of the material. Typically, a w/c ratio of 0.35–0.50 is used to

achieve a balance between flowability and strength. While increasing the water content enhances workability and flowability, it can lead to lower strength and greater shrinkage after curing. Therefore, careful control of the w/c ratio is essential to ensure the mix is both extrudable and structurally sound.

5.2.8 Water-to-Cement Ratio (w/c)

The water-to-cement ratio (w/c) is one of the most critical factors in 3DPC, directly influencing the strength and durability of the printed material. A lower w/c ratio (typically around 0.35–0.40) results in higher strength and lower shrinkage but can negatively impact the workability and extrudability of the material. Conversely, a higher w/c ratio increases flowability, making the material easier to extrude but often at the cost of lower compressive strength and increased shrinkage. Therefore, finding the optimal w/c ratio is key to ensuring both printability and the long-term performance of the printed structure.

5.2.9 Impact of Viscosity Modifying Agents (VMA) on 3D Printable Concrete (3DPC)

Viscosity Modifying Agents (VMA) are essential additives in 3D printable concrete (3DPC) as they significantly influence the material's rheological properties, including flowability, extrudability, and shape retention. VMAs work by modifying the yield stress and viscosity of the fresh mix, which directly affects the printability and buildability of the material during the 3D printing process.

The addition of VMA enhances the workability and stability of the mix by increasing its viscosity, which helps prevent segregation and slumping of the material after extrusion. This characteristic is particularly important for printing overhangs and vertical layers, where the material must maintain its form without excessive deformation or collapse. By improving the stability

of the printed layers, VMAs contribute to a more controlled extrusion process, ensuring consistent layer deposition and structural integrity.

However, while VMA improves layer stability, excessive amounts can negatively impact extrudability. An increase in viscosity beyond the optimal range can lead to blockages in the nozzle or difficulty in pumping the mix, which may hinder the extrusion process. Therefore, it is crucial to find an optimal balance between VMA dosage and superplasticizer content. This balance ensures sufficient viscosity enhancement for stability, without reducing the flowability needed for smooth extrusion. In general, the careful use of VMA, along with other admixtures like superplasticizers, is key to achieving a viscous yet extrudable mix, which is essential for successful 3D concrete printing.

5.3 Mixing Process for 3D Concrete Printable Mix

The 3D concrete printable (3DCP) mix was prepared using a **pump-integrated 3DCP concrete mixer**, designed to achieve optimal consistency and homogeneity in the mixture. The process was carefully segmented to ensure thorough integration of all components, including dry ingredients, liquid additives like superplasticizer (SP), viscosity-modifying agents (VMA), and nano-clay.

5.3.1 Preparation of Liquid Mix

The preparation of the liquid mix was a crucial first step. Water, superplasticizer (SP), and viscosity-modifying agent (VMA) were combined to create a homogeneous liquid mixture. This blend was mixed in a Hobart planetary-type mixer for 5 minutes or until a thick paste was formed. Once the paste reached the desired consistency, it was transferred to the mixing hopper, where it was allowed to rest for 15 minutes to ensure

even dispersion and sufficient chemical interaction between the components.

5.3.2 Dry Ingredient Mixing

In parallel, the dry ingredients—cement, sand, S, and FA are prepared and added to the mixer in a slow, controlled manner over a period of 10 minutes. This slow addition prevented clumping and ensured the even distribution of all dry materials. The dry mix was carefully integrated into the system to maintain a uniform consistency.

5.3.3 Addition of Nano-Clay

For mixes that included nano-clay, a portion of the mixing water (approximately 15%) was reserved separately from the main liquid blend. The nano-clay particles are then sprinkling on this reserved water-cement mix. This step was essential to ensure the even dispersion of nano-clay particles, which can otherwise be difficult to incorporate uniformly due to their fine size. After 5 minutes, the prepared nano-clay suspension was added into the main mixer.

5.3.4 Final Mixing and Blending

Once the nano-clay suspension was added, the mixing process continued with the blades rotating at a speed of 360 RPM for a period of 24 minutes. The high-speed mixing ensured that the mix achieved a homogeneous consistency, and the components were fully integrated. This extended mixing duration was crucial for achieving the correct rheological properties required for 3D printing, ensuring that the mix could flow smoothly and be extruded effectively while maintaining its shape.

5.3.5 Batch Production

Each batch of the prepared 3DCP mix produced approximately 100 kg of material. This amount was sufficient for use in 3D printing applications, ensuring that the mix had the desired properties for extrusion and buildability. The mix was monitored throughout the preparation process to ensure the required flowability and consistency were met, making it suitable for printing complex geometries.

5.4 Printing Tests:

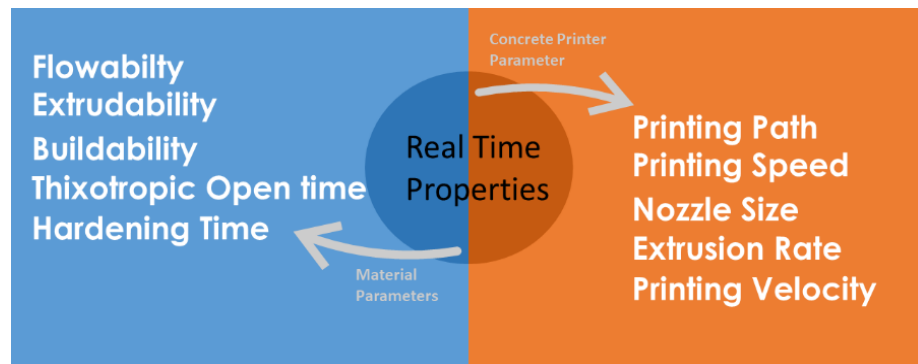


Figure 32 Real-time properties of 3DCP

Concrete 3D printing represents an emerging technology yet to be widely adopted commercially. (Giridhar et al., 2023b) Consequently, standardized testing protocols and guidelines are currently lacking, posing significant challenges for the precise design of printable concrete mixes aimed at achieving targeted mechanical strengths. Through an extensive literature review combined with rigorous experimental investigations, specific test methodologies have been identified that accurately evaluate critical parameters such as flowability, printability, and extrudability of printable concrete mixtures. Additionally, efforts have been directed toward developing concrete mix designs capable of reliably predicting the mechanical performance of 3D-printed structural elements.

5.4.1 Extrudability Test:



Figure 33 Illustrate Extrudability- PASS (Smooth surface and continuous print)

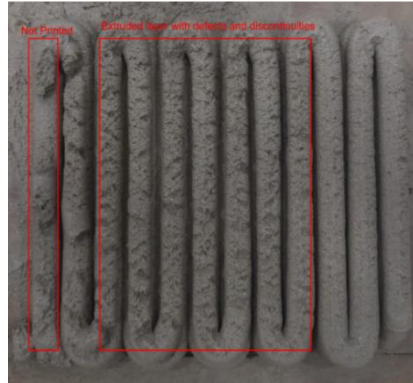


Figure 34 Illustrate Extrudability- FAIL (Contains lots of voids and defects)

Before initiating the printing of any structural element, it is imperative to conduct an extrudability test. Extrudability is defined as the capability of a concrete mixture to be consistently extruded through the printer nozzle, maintaining dimensional accuracy and producing defect-free layers. Defect-free, in this context, refers specifically to the absence of voids, cracks, discontinuities, or any visible irregularities in the printed material. The evaluation of print quality was performed primarily through visual inspection. For the extrudability test procedure, a single-layer line, measuring 30 cm in length, was extruded using the designated nozzle size and print speed.(Rahul et al., 2022) The width and height of the printed layers are measured for every 10 cm at the printed layer. The test considered successful ("pass") if two specific criteria were met: (i) all dimensional measurements corresponded accurately to the dimensions of the circular nozzle printed layer by 20mm nozzle with an layer width of 25mm within an allowable acceptance of approximately 0.5 mm variation, and (ii) the extruded line exhibited no surface defects, including voids or discontinuities. Fig. 13 and fig.14 are the images that demonstrated the pass and fail mix designs,

5.4.2 Buildability Test:

During the additive manufacturing process, the printed object must maintain self-supporting capabilities without reliance on conventional rigid formworks. Fresh concrete needs to withstand gravity loads post-deposition, including its own weight and subsequent layers. This capability, termed "buildability" (Rahul et al., 2019a), is crucial. However, due to inferior material properties in early hydration stages, 3D printed concrete often exhibits inadequate buildability, leading to dimensional inaccuracies and unstable failure modes. Two primary structural failure mechanisms identified in 3D concrete printing are elastic buckling and plastic collapse. Therefore, buildability is a critical parameter in designing and optimizing 3D printed concrete components.

The approach proposed by Kazemian et al. (2017) was utilized to evaluate the buildability of deposited layers. Two consecutive layers of the concrete sample were printed without any time gap between them for testing purposes. The compression of the bottom layer after printing the upper second layer was measured. The timing between layers was determined based on the specific element being printed. The research undertaken at IIT Indore aimed to develop a layer-wise extrudable mixture for additive manufacturing of structures, facilitating continuous printing without pauses, thereby reducing overall construction time. The printed specimens are rectangular cylinders with a filament layer thickness of 25mm. It is printed through the nozzle size of 20mm. In this case, the slabs of 300x300x70mm are cast. It is a 6-layer slab with a nozzle diameter of 20mm, which can give a print of 25mm in width. The printing speed is 3600mm/min. The time gap between the first layer and the above printing of the layer is around 2 minutes.

During the printing process, the fresh layers were closely observed for any signs of deformation or instability. In particular, the vertical deformation (settlement/compression) of the first layer was measured immediately before and after placing the second layer. This was done by recording the first layer's thickness at multiple points and determining the average reduction in height, which served as a quantitative indicator of buildability (i.e. the capacity of the material to support subsequent layers without

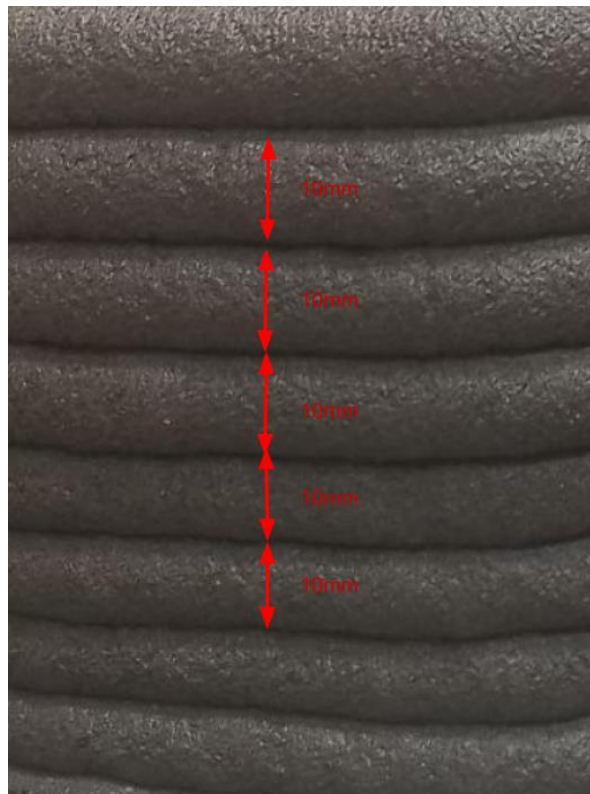


Figure 35 illustration of Buildability Test- Same width of Layers

significant collapse or shape loss). A similar qualitative observation was extended to the multi-layer rectangle shape and circularaafter printing all six layers, the geometry of the lower layers was inspected for any sagging or distortion under the weight of the overlying material. The absence of noticeable distortion in the base layers indicated good structural stability of the printed element.



Figure 36 Illustrate image for Buildability- PASS (Smooth surface and continuous print)



Figure 37 Illustrate image for Buildability- PASS (Smooth surface and continuous print)



Figure 38 Illustrate image for Buildability- FAIL (Not Extrudable slump, Stiff)



Figure 39 Illustrate image for Buildability- FAIL (Overflow and collapsible slump)

In the study, the numerous trials have done. Many mix design trial checked to attained the buildability of 3DCP mix. Figure 17 demonstrates that the buildability of the mix is perfect. It is printed continuously without the time gap. The total layer printed is 12 layers in rectangular shape printing. While for the cylindrical shape printing, the continuous layer-by-layer printing withstands up to 9 layers.

Fig. 20, demonstrates that the mix deigned is not extrudable and buildable. It shows defects, interrupted layer deposition, rough surface, and various

cracks over the surface of extruded layer. Fig. 21 demonstrates the mix had poor buildability strength and collapse within only 4 layers. The failure of the mix is due to the increase in the W/C ratio and improper proportions of superplasticizer in the mix design.

5.4.3 Open Time Test

Open time refers to the period during which 3D printable concrete (3DPC) remains flowable and can be extruded through the nozzle without clogging or blockage. For optimal printability, the open time must be longer than the extrusion time to ensure that the material maintains its workability and is successfully deposited in layers. The end of open time is typically marked when the material begins to lose extrudability due to an increase in yield stress and viscosity. Key challenges, such as cold joints and filament disruptions, arise when the material sets too quickly, which can lead to poor bonding between layers and structural integrity issues.

To evaluate open time, several testing methods are employed, which focus on measuring changes in the material's flowability over time. Common tests include the shear stress test, flow table test, Vicat apparatus, and rheometer tests. Researchers have also used slump tests and V-Funnel tests to determine changes in workability. For research, (Tarhan & Şahin, 2021b) used the Vicat apparatus to track flowability, while (Malaeb et al., 2019) employed the slump test. Other studies, such as those by (Y. Chen, Jansen, et al., 2020), assessed pumping and extrusion capacity to determine when the material no longer maintains smooth flow due to increased yield stress, marking the end of open time.

5.4.3.1 Practical Approaches for Determining Open Time

(Y. Chen, Jansen, et al., 2020) proposed a practical approach for determining open time by defining it as the period during which the material can be extruded smoothly, without interruptions or discontinuities. This

method emphasizes the practical observation of the material's behavior



Figure 40 End of open time with interruption and rough surface of filaments after 2min of printing

during the extrusion process. Additionally, figures from recent studies demonstrate how the material's **flowability** decreases over time. For example, **Fig. 11** illustrates a decrease in filament width and initiation of voids and cracks in the extrudable filament, showing that the material's **flowability** diminishes as the open time progresses. Eventually, the material becomes unable to extrude a continuous filament, marking the **end of open time** . After this condition the material begins to **block** the nozzle as **yield stress** increases over time .

5.4.3.2 Factors Affecting Open Time

The sand weight ratio and the inclusion of various **admixtures** can significantly influence the **open time** of 3D printable concrete (3DPC). The **mixing proportions** of **superplasticizer (SP)** and **viscosity-modifying agents (VMA)** play a crucial role in determining the **open time test (OTT)**. As the **superplasticizer** content increases, it enhances the **flowability** of the paste, extending the **open time**. However, the amount of **SP** should not exceed **0.1% of the cement content**, as excessive amounts can lead to a **decrease in yield strength** of the fresh 3DPC mixture. Additionally, while the inclusion of **silica** enhances the properties of 3DPC, excessive silica content can negatively impact **extrudability**. It is generally recommended that silica content be maintained between **3% and 4%** of the mix. Exceeding this range can necessitate a higher proportion of **superplasticizer**, which may further reduce the **yield strength** of the **hardened 3DPC structures**.

Panda and Tan (2018) found that a higher content of GGBS slag (15%) reduced open time, as the material set faster compared to mixes with 5% GGBS, which exhibited longer open times. In contrast, Bong et al. (2020) demonstrated that the Si/Na ratio in geopolymer-based mixes had a significant impact on the open time. They also observed that K-based activators led to shorter open times than Na-based activators, due to faster reactions between Si and Al oligomers.

The inclusion of **retarders**, such as **tartaric acid**, has been found to effectively extend the open time by preventing premature setting. (Y. Chen, Jansen, et al., 2020) reported that a **0.30% dosage** of retarder increased the open time significantly, while higher dosages of retarders, such as **1%**, reduced the open time to around 20 minutes compared to **0.5% dosage**. This was further supported by the findings of (Nerella et al., 2020), who

concluded that **retarders** could be added after mixing to prevent early setting, whereas **accelerators** should be introduced prior to extrusion .

5.5 Mix Proportions of Studied Trial

Table 2: Mix Proportions of Studied Trial

Name	Cement	Silica fume	Fly ash	Clay	Sand	SP	Water	VMA	VMA(%) of cement	Remark
3DCPTL01	750	0	0	8.75	1080	0.6	376	9.75	1.3	Non printable-True Slump
3DCPTL02	750	0	0	8.75	1080	0.6	376	6.375	0.85	Non printable-True Slump
3DCPTL03	750	0	0	8.75	1080	0.6	376	4.85	0.65	Non Printable-14cm flow
3DCPTL04	750	0	0	8.75	1080	0.6	376	3.9	0.52	Non-Printable-15 cm flow
3DCPTL05	750	0	0	8.75	1080	0.6	376	2.925	0.39	Non Printable- Due to VMA stickiness-17cm flow
3DCPTL06	750	0	0	8.75	1080	0.6	376	1.95	0.26	Good mix with little stickiness(approx.20 cm)
3DCPTL07	750	0	0	8.75	1080	0.6	376	0.975	0.13	Good mix (approx.21 cm)
3DCPTL08	750	0	0	8.75	1080	0.6	376	0.975	0.08%	Good mix (approx.21 cm)
3DCPTL09	750	0	0	8.75	1080	1.2	376	0.975	0.16	Good mix with increased setting time (approx. slump flow 17 cm)
3DCPTL10	750	0	0	8.75	1080	2.4	376	0.975	0.32	Good mix with increased setting time (approx. slump flow 19 cm)
3DCPTL11	750	0	0	8.75	1080	4.8	376	0.975	0.64	Good mix, Extrudable, Buildable up to 3 layers (approx. slump flow 19 cm)
3DCPTL12	750	0	0	8.75	1080	9.6	376	0.975	1.28	Good mix, Extrudable, Not Buildable (approx.slump flow 19 cm)
3DCPTL13	750	0	0	8.75	1080	11.25	376	0.975	1.5	Self Settleable property, Not Buildable
3DCPTL14	750	0	0	8.75	1080	15	376	0.975	2	Self-flow property, not extrudable, and not Buildable

5.6 Preparation of Test Specimen

The 3DCP casted slab specimens are prepared of size 300mm x300x70mm. For the testing of printed concrete, specimens were cut out from the slab, as



Figure 41 Cutting of slab into cubes- 50x50x50mm



Figure 42 Cutting of slab in beam- 160x40x40mm

explained in Fig. 37. Four such slabs were cast and cut to get a sample of 9 cubes and 12 beams. It should be noted that cutting may generate small

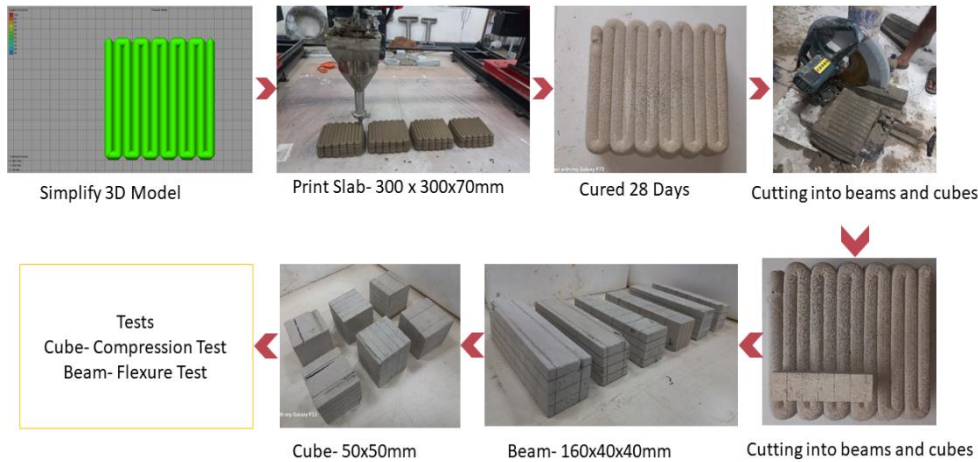


Figure 43 Flow chart of the samples making procedure

microcracks in the specimens, adversely affecting the strength. To avoid such cases, a diamond saw cutter is suitable. The slab is 300mm x 300 mm with 12 layers horizontally and seven layers vertically, with a time gap of only 2 minutes, and is printed. The current project at IIT Indore is to formulate a printable mixture for additive Manufacturing for optimized beam structures and identify its compressive strength. The mix is suitable for an extrusion speed of 3600 mm/min for an extruder-based 3D concrete

printer. It takes approximately 7 minutes for each slab to print. For the four slabs, it takes approximately. 24-30 minutes.

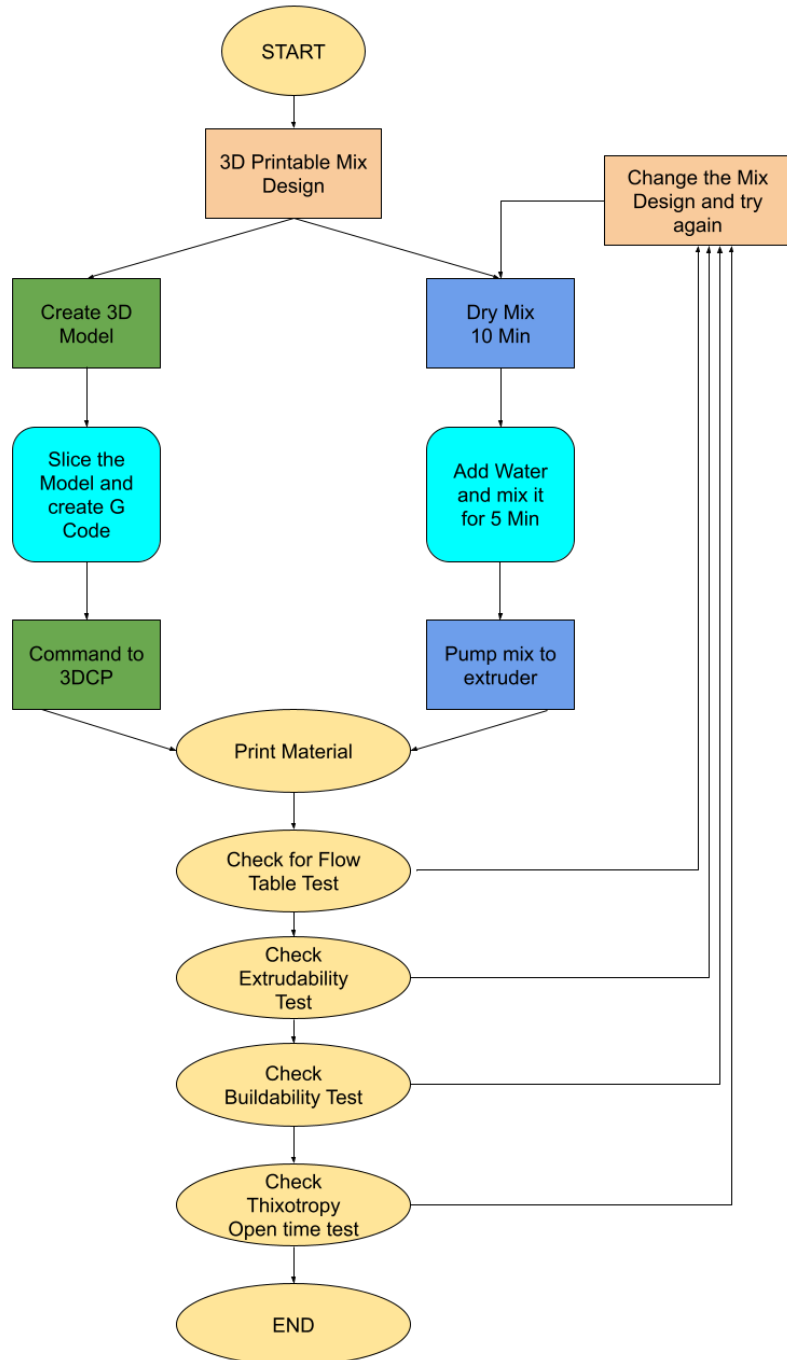


Figure 44 Schematic diagram for the steps to be carried out during 3D concrete printing

5.7 Mechanical Properties Test and Results

The samples are cast and cut into cubes and beams as shown in Fig. 37. The samples are marked with a permanent marker to highlight the layer printing layer and loading directions. The nomenclature is done according to the printing and loading directions

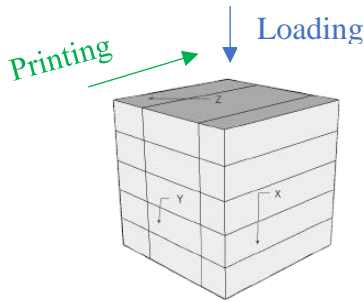


Figure 45 Sample CSZX01

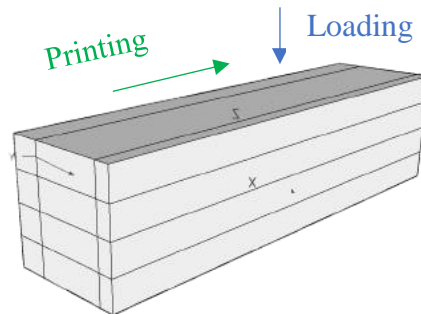


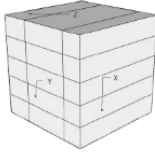

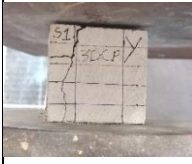
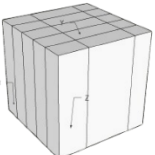


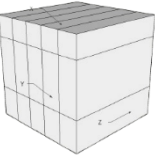


Figure 46 Sample FSZX01

The third term reflects the plane perpendicular to the loading direction, and the fourth reflects its front view. For example, for CSZX01, the 'Z' is the loading plane, and the 'X-plane' is on the front side. Fig. 39. Loading direction and printing direction of the beam are shown in Fig. 38.

5.7.1 Compression Strength Test

To determine the compressive strength, cubes of 50x50x50mm size are cut from the slab shown in Fig. 35. It is tested in the three directions, as shown in the table. The location from which the cube is cut is shown in Fig. 35. Since the cube is extracted from the middle portion of the slabs, the edges of the slabs are removed by the cutter. At the same time, the mould-casted cubes are also prepared. The direction of loading is shown in Fig. 39. Each sample is tested for every loading and printing direction to obtain accurate results.

Table 3: Compression Test Results

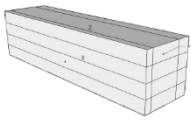

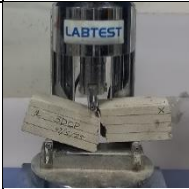
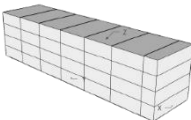


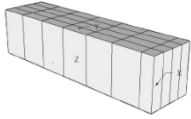


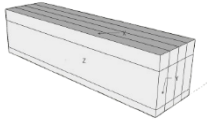


Sr. No.	Sample	3D Model	Actual Model	After Testing	Compressive Strength (MPa)	Standard Deviation
1	CSZX01				22	2.45
2	CSYX02				24	1.63
3	CSXZ03				20.8	2.16

5.7.2 Flexure Strength Test

The Flexure strength test results are shown in table no. X. The flexure strength test. The specimens are extracted from the slabs shown in fig. 34. The loading and printing directions are shown in Fig. 34. There are four

possible different directions for testing the beam. The test results are described in Table No. X

Table 4: Flexure Test Results

Sr. No.	Sample	3D Model	Actual Model	After Testing	Flexure Strength	Standard Deviation
1	FSZX01				3.678	4.08
2	FSZY02				3.592	2.054
3	FSX 03				3.384	1.632
4	FSY 04				2.967	4.189

Chapter 6

Results and Discussion

6.1 Fresh 3DCP Mix Design

6.1.1 True Slump: Unfit for 3DCP

True slump refers to a stiff concrete mix that lacks the necessary flowability for smooth extrusion in 3D printing applications. A true slump is characterized by a rigid mix that does not maintain its shape during the extrusion process, leading to inconsistent prints and potential clogging issues in the printer nozzle. For example, samples such as 3DCPTL01, 3DCPTL02, 3DCPTL03, and 3DCPTL04 exhibited a true slump, with remarks like "Non printable-True Slump," indicating that these mixes were too stiff for 3DCP. These mixes have flow values that are too low (below 19 cm), making them unsuitable for the precise deposition required in 3D printing.

6.1.2 Ideal Flowability for 3DCP (19 to 22 cm)

The critical flow range for a 3D concrete printable mix is typically between 19 cm and 22 cm. This range ensures that the concrete mix is neither too stiff nor too runny, striking the right balance for extrusion. Mixes with flow values within this range can maintain structural integrity while being extruded through the nozzle and upon deposition. For example, the mixes 3DCPTL06, 3DCPTL07, and 3DCPTL08 exhibited flowability values around 20 cm (with slight variations), marked as "Good mix (approx. 21 cm)." These mixes demonstrated ideal flow characteristics for 3DCP, where

the material could flow smoothly during extrusion without collapsing or failing to maintain its printed form.

The remark "Good mix with little stickiness (approx. 20 cm)" for sample 3DCPTL06 suggests that the mix could be extruded smoothly while still maintaining the necessary structural properties for 3D printing. Similarly, 3DCPTL07, with a flow value around 21 cm, was noted as "Good mix (approx. 21 cm)," confirming its suitability for additive manufacturing applications where precise control over each layer is crucial.

6.1.3 Effect of VMA (Viscosity Modifying Agent)

Viscosity Modifying Agents (VMA) are essential in adjusting the rheological properties of the mix, particularly its flowability. When the VMA concentration is appropriately adjusted, it helps in optimizing the concrete's workability for 3D printing. In the case of 3DCPTL05, a VMA of 2.925% resulted in a mix that was non-printable due to excessive stickiness, as described by the remark "Non Printable- Due to VMA stickiness-17cm flow." The increased stickiness in this case hindered smooth extrusion and the ability to maintain the intended shape of the printed layers.

Conversely, lower VMA concentrations in mixes like 3DCPTL06 (0.26% VMA) and 3DCPTL07 (0.13% VMA) allowed for improved flowability and printability, within the ideal range of 19 to 22 cm. This range is key to ensuring that the concrete flows smoothly but does not lose its structural integrity after extrusion.

6.1.4 Setting Time and Buildability

In 3DCP, setting time plays a significant role in ensuring that the concrete mix can support successive layers. A slower setting time allows for greater control during the printing process and ensures better bonding between

layers. The samples 3DCPTL09 and 3DCPTL10, with increased setting times (due to higher VMA content), were marked as "Good mix with increased setting time (approx. slump flow 17 cm)" and "Good mix with increased setting time (approx. slump flow 19 cm)," respectively. These mixes were suitable for 3DCP applications where more time was needed for precise layer deposition and fine control over the printed object.

In some cases, a higher VMA content improved the extrudability and buildability of the mix, as seen in 3DCPTL11, which was deemed "Good mix, Extrudable, Buildable up to 3 layers (approx. slump flow 19 cm)." This indicates that the mix could be used for printing objects with multiple layers without losing its structural integrity.

6.1.5 Self-Settling and Non-Buildable Mixes

Finally, mixes like 3DCPTL13 and 3DCPTL14, while having self-settling properties, were deemed "Not Buildable" due to their inability to support additional layers. These mixes, with flowability values above 22 cm (e.g., 3DCPTL14 with 15 cm slump flow), were classified as "Self-flow property, not extrudable, and not Buildable." While they could self-level, making them suitable for applications where precision and layering were not critical, they were not suitable for multi-layered 3D printing, as the material could not support its own weight during deposition.

6.2 Predictions by ML Models

This research explores how various factors, such as SP, VMA, W/B, and loading direction, affect the compressive strength (CS) and flexural strength (FS) of printable 3D concrete using machine learning (ML) algorithms. To ensure accuracy, the data arrangement and cleaning has been done. Five resilient machine learning models are been used. These are Random Forest (RF), XGBoost, Decision Trees (DT), Gradient Boosting Machine (GBM)

and Support Vector Machine (SVM). These models were applied to forecast the CS for 3DCP, providing a detailed assessment of their performance. The optimal linear equation derived from the model can be implemented in practical situations. The evaluation of ML model accuracy is been demonstrated by the parameters R^2 , MSE , MAE , $RMSE$ and $SMAPE$ for compression strength and flexure strength prediction. 3 ML models, i.e., RF, Compact GBM, and Compact RF, predict approximately similar values during training, R^2 displays a Compressive strength of 0.84. The MAPE values of RF, Compact GBM, and Compact RF are 21.89%, 25.97%, and 23.69%, respectively. However, for MAPE, the best model is GB, which has a value of 21.18%. The subsequent ranks are RF > Compact RF > GBM > Compact GBM > SVM > DT > ANN are according to their accuracy for compressive strength prediction.

6.3 Mechanical Test Results

A total of 14 mix trials (labeled 3DCPTL1 to 3DCPTL14) were performed to evaluate the flowability, extrudability, open time, and buildability of the mixes. The mixes that satisfied the printability criteria were 3DCPTL08, 3DCPTL09, and 3DCPTL10. These specific mixes were used to establish optimal proportions for 3DCP while maintaining consistent printing parameters. Mix 3DCPTL08, comprising 29.2% OPC, 6.44% fly ash, 6.44% silica fume, 0.93% limestone powder, 0.6% SP, and 0.975% VMA, demonstrated crucial characteristics such as buildability, extrudability, setting time, mix cohesion, reduced deformation, and efficient control of cement hydration.

The fresh and hardened properties of the printable mix 3DCPTL08 included a flow value of 210 mm, an open time of 25 minutes, an initial setting time of 105 minutes, and a final setting time of 110 minutes. After 28 days, the compressive strength of the printed specimen in the X, Y, and Z directions was measured to be 22.24, 20.47, and 20.8 MPa, respectively.

3DCPTL08 involved a nozzle size of either 20 or 25 mm, with an extrusion speed of 3600 mm/min. The 14 mix trials (3DCPTL01 to 3DCPTL14) were designed to assess flowability, extrudability, open time, and buildability. The mixes 3DCPTL08, 3DCPTL09, and 3DCPTL10 met the printability criteria.

Chapter 7

FUTURE SCOPE

Future research in 3D concrete printing (3DCP) should explore advanced machine learning techniques such as reinforcement learning and ensemble methods to optimize predictive models for material properties and printing parameters. Enhancing sustainability metrics with comprehensive life cycle assessment (LCA) alongside carbon footprint predictions will be crucial for developing environmentally sustainable 3DCP practices. Implementing real-time monitoring and control systems using IoT devices and sensors can improve process efficiency and error reduction. Investigating multi-material and functionally graded structures will push the boundaries of architectural applications. Establishing standardized testing protocols and regulatory frameworks specific to 3DCP materials and structures will ensure safety and reliability in construction. Collaborative research initiatives and partnerships between academia, industry, and government will accelerate innovation and adoption of 3DCP technologies. Economic analyses and market studies are essential to assess the cost-effectiveness and market potential of 3DCP compared to traditional construction methods, while specialized education and training programs will prepare the workforce for implementing advanced 3DCP solutions. Validating the results predicted from the ML algorithms about the compression test by performing the UCS on elements casted by 3D printed mix samples. Analyzing it for other mechanical properties like tensile test, pull-out test, high and low-velocity impact test, and temperature tests will provide comprehensive insights into the structural performance and durability of 3D-printed concrete in various real-world conditions.

Chapter 8

REFERENCES

1. *A Data-Driven Design for Fault Detection of Wind Turbines Using Random Forests and XGboost* / IEEE Journals & Magazine / IEEE Xplore. (n.d.). Retrieved 17 May 2025, from <https://ieeexplore.ieee.org/document/8329419>
2. Agrawal, A. K., & Chakraborty, G. (2021). On the use of acquisition function-based Bayesian optimization method to efficiently tune SVM hyperparameters for structural damage detection. *Structural Control and Health Monitoring*, 28(4), e2693. <https://doi.org/10.1002/STC.2693> ;SUBPAGE:STRING:FULL
3. Albar, A., Chougan, M., Al- Kheetan, M. J., Swash, M. R., & Ghaffar, S. H. (2020). Effective extrusion-based 3D printing system design for cementitious-based materials. *Results in Engineering*, 6. <https://doi.org/10.1016/j.rineng.2020.100135>
4. Ayat, N. E., Cheriet, M., & Suen, C. Y. (2005). Automatic model selection for the optimization of SVM kernels. *Pattern Recognition*, 38(10), 1733–1745. <https://doi.org/10.1016/J.PATCOG.2005.03.011>
5. Bakouregui, A. S., Mohamed, H. M., Yahia, A., & Benmokrane, B. (2021). Explainable extreme gradient boosting tree-based prediction of load-carrying capacity of FRP-RC columns. *Engineering Structures*, 245, 112836. <https://doi.org/10.1016/J.ENGSTRUCT.2021.112836>
6. Baz, B., Aouad, G., & Remond, S. (2020). Effect of the printing method and mortar's workability on pull-out strength of 3D printed elements. *Construction and Building Materials*, 230. <https://doi.org/10.1016/j.conbuildmat.2019.117002>
7. Bong, S. H., Xia, M., Nematollahi, B., & Shi, C. (2021). Ambient temperature cured 'just-add-water' geopolymer for 3D concrete printing applications. *Cement and Concrete Composites*, 121. <https://doi.org/10.1016/j.cemconcomp.2021.104060>
8. Chaves Figueiredo, S., Romero Rodríguez, C., Ahmed, Z. Y., Bos, D. H., Xu, Y., Salet, T. M., Çopuroğlu, O., Schlangen, E., & Bos, F. P. (2019). An approach to develop printable strain hardening

- cementitious composites. *Materials and Design*, 169. <https://doi.org/10.1016/j.matdes.2019.107651>
9. Chen, M., Guo, X., Zheng, Y., Li, L., Yan, Z., Zhao, P., Lu, L., & Cheng, X. (2018). Effect of tartaric acid on the printable, rheological and mechanical properties of 3D printing sulphoaluminate cement paste. *Materials*, 11(12). <https://doi.org/10.3390/ma11122417>
 10. Chen, M., Li, L., Wang, J., Huang, Y., Wang, S., Zhao, P., Lu, L., & Cheng, X. (2020). Rheological parameters and building time of 3D printing sulphoaluminate cement paste modified by retarder and diatomite. *Construction and Building Materials*, 234. <https://doi.org/10.1016/j.conbuildmat.2019.117391>
 11. Chen, M., Li, L., Zheng, Y., Zhao, P., Lu, L., & Cheng, X. (2018). Rheological and mechanical properties of admixtures modified 3D printing sulphoaluminate cementitious materials. *Construction and Building Materials*, 189, 601–611. <https://doi.org/10.1016/j.conbuildmat.2018.09.037>
 12. Chen, M., Yang, L., Zheng, Y., Huang, Y., Li, L., Zhao, P., Wang, S., Lu, L., & Cheng, X. (2020). Yield stress and thixotropy control of 3D-printed calcium sulfoaluminate cement composites with metakaolin related to structural build-up. *Construction and Building Materials*, 252. <https://doi.org/10.1016/j.conbuildmat.2020.119090>
 13. Chen, T., & Guestrin, C. (2016). XGBoost: A scalable tree boosting system. *Proceedings of the ACM SIGKDD International Conference on Knowledge Discovery and Data Mining, 13-17-August-2016*, 785–794. https://doi.org/10.1145/2939672.2939785/SUPPL_FILE/KDD2016_CHEN_BOOSTING_SYSTEM_01-ACM.MP4
 14. Chen, Y., Chaves Figueiredo, S., Li, Z., Chang, Z., Jansen, K., Çopuroğlu, O., & Schlangen, E. (2020). Improving printability of limestone-calcined clay-based cementitious materials by using viscosity-modifying admixture. *Cement and Concrete Research*, 132. <https://doi.org/10.1016/j.cemconres.2020.106040>
 15. Chen, Y., He, S., Zhang, Y., Wan, Z., Çopuroğlu, O., & Schlangen, E. (2021). 3D printing of calcined clay-limestone-based cementitious materials. *Cement and Concrete Research*, 149. <https://doi.org/10.1016/j.cemconres.2021.106553>
 16. Chen, Y., Jansen, K., Zhang, H., Romero Rodriguez, C., Gan, Y., Çopuroğlu, O., & Schlangen, E. (2020). Effect of printing parameters on interlayer bond strength of 3D printed limestone-calcined clay-based cementitious materials: An experimental and

- numerical study. *Construction and Building Materials*, 262, 120094. <https://doi.org/10.1016/J.CONBUILDMAT.2020.120094>
17. Chen, Y., Romero Rodriguez, C., Li, Z., Chen, B., Çopuroğlu, O., & Schlangen, E. (2020). Effect of different grade levels of calcined clays on fresh and hardened properties of ternary-blended cementitious materials for 3D printing. *Cement and Concrete Composites*, 114. <https://doi.org/10.1016/j.cemconcomp.2020.103708>
 18. Chen, Y., Zhang, Y., Pang, B., Liu, Z., & Liu, G. (2021). Extrusion-based 3D printing concrete with coarse aggregate: Printability and direction-dependent mechanical performance. *Construction and Building Materials*, 296. <https://doi.org/10.1016/j.conbuildmat.2021.123624>
 19. Chou, J. S., Tsai, C. F., Pham, A. D., & Lu, Y. H. (2014). Machine learning in concrete strength simulations: Multi-nation data analytics. *Construction and Building Materials*, 73, 771–780. <https://doi.org/10.1016/J.CONBUILDMAT.2014.09.054>
 20. Chu, S. H., Li, L. G., & Kwan, A. K. H. (2021). Development of extrudable high strength fiber reinforced concrete incorporating nano calcium carbonate. *Additive Manufacturing*, 37. <https://doi.org/10.1016/j.addma.2020.101617>
 21. Cicione, A., Kruger, J., Walls, R. S., & Van Zijl, G. (2021). An experimental study of the behavior of 3D printed concrete at elevated temperatures. *Fire Safety Journal*, 120. <https://doi.org/10.1016/j.firesaf.2020.103075>
 22. Ding, T., Xiao, J., Zou, S., & Wang, Y. (2020). Hardened properties of layered 3D printed concrete with recycled sand. *Cement and Concrete Composites*, 113. <https://doi.org/10.1016/j.cemconcomp.2020.103724>
 23. Ding, T., Xiao, J., Zou, S., & Zhou, X. (2020). Anisotropic behavior in bending of 3D printed concrete reinforced with fibers. *Composite Structures*, 254. <https://doi.org/10.1016/j.compstruct.2020.112808>
 24. du Plessis, A., Babafemi, A. J., Paul, S. C., Panda, B., Tran, J. P., & Broeckhoven, C. (2021). Biomimicry for 3D concrete printing: A review and perspective. *Additive Manufacturing*, 38, 101823. <https://doi.org/10.1016/J.ADDMA.2020.101823>
 25. Fernández-Altable, V., & Casanova, I. (2006). Influence of mixing sequence and superplasticiser dosage on the rheological response of cement pastes at different temperatures. *Cement and Concrete*

- Research*, 36(7), 1222–1230.
<https://doi.org/10.1016/J.CEMCONRES.2006.02.016>
26. Gao, J., Wang, C., Li, J., & Chu, S. H. (2024). Data-driven rheological model for 3D printable concrete. *Construction and Building Materials*, 447.
<https://doi.org/10.1016/j.conbuildmat.2024.137912>
 27. Geng, S. Y., Mei, L., Cheng, B. Y., Luo, Q. L., Xiong, C., & Long, W. J. (2024). Revolutionizing 3D concrete printing: Leveraging RF model for precise printability and rheological prediction. *Journal of Building Engineering*, 88, 109127.
<https://doi.org/10.1016/J.JOBE.2024.109127>
 28. Ghasemi, A., & Naser, M. Z. (2023). Tailoring 3D printed concrete through explainable artificial intelligence. *Structures*, 56, 104850.
<https://doi.org/10.1016/J.ISTRUC.2023.07.040>
 29. Giridhar, G., Prem, P. R., & Kumar, S. (2023a). Development of concrete mixes for 3D printing using simple tools and techniques. *Sadhana - Academy Proceedings in Engineering Sciences*, 48(1), 1–13. <https://doi.org/10.1007/S12046-022-02069-W/FIGURES/12>
 30. Giridhar, G., Prem, P. R., & Kumar, S. (2023b). Development of concrete mixes for 3D printing using simple tools and techniques. *Sadhana - Academy Proceedings in Engineering Sciences*, 48(1), 1–13. <https://doi.org/10.1007/S12046-022-02069-W/FIGURES/12>
 31. Hengl, T., Leenaars, J. G. B., Shepherd, K. D., Walsh, M. G., Heuvelink, G. B. M., Mamo, T., Tilahun, H., Berkhout, E., Cooper, M., Fegraus, E., Wheeler, I., & Kwabena, N. A. (2017). Soil nutrient maps of Sub-Saharan Africa: assessment of soil nutrient content at 250 m spatial resolution using machine learning. *Nutrient Cycling in Agroecosystems*, 109(1), 77–102.
<https://doi.org/10.1007/S10705-017-9870-X/FIGURES/12>
 32. Heras Murcia, D., Genedy, M., & Reda Taha, M. M. (2020). Examining the significance of infill printing pattern on the anisotropy of 3D printed concrete. *Construction and Building Materials*, 262. <https://doi.org/10.1016/j.conbuildmat.2020.120559>
 33. Huang, F., Li, H., Yi, Z., Wang, Z., & Xie, Y. (2018). The rheological properties of self-compacting concrete containing superplasticizer and air-entraining agent. *Construction and Building Materials*, 166, 833–838.
<https://doi.org/10.1016/j.conbuildmat.2018.01.169>
 34. Hwang, H.-J., Sakai, E., & Lee, S.-H. (2009). Rheological behavior of a slag cement paste prepared by adjusting the particle size

- distribution. *Journal of Ceramic Processing Research*, 10(4), 409–413. <https://doi.org/10.36410/JCPR.2009.10.4.409>
35. Izadgoshasb, H., Kandiri, A., Shakor, P., Laghi, V., & Gasparini, G. (2021). Predicting compressive strength of 3D printed mortar in structural members using machine learning. *Applied Sciences (Switzerland)*, 11(22). <https://doi.org/10.3390/APP112210826>
 36. Kavzoglu, T., & Teke, A. (2022). Advanced hyperparameter optimization for improved spatial prediction of shallow landslides using extreme gradient boosting (XGBoost). *Bulletin of Engineering Geology and the Environment*, 81(5), 1–22. <https://doi.org/10.1007/S10064-022-02708-W/METRICS>
 37. Kawashima, S., Chaouche, M., Corr, D. J., & Shah, S. P. (2013). Rate of thixotropic rebuilding of cement pastes modified with highly purified attapulgite clays. *Cement and Concrete Research*, 53, 112–118. <https://doi.org/10.1016/J.CEMCONRES.2013.05.019>
 38. Kazemian, A., Yuan, X., Cochran, E., & Khoshnevis, B. (2017). Cementitious materials for construction-scale 3D printing: Laboratory testing of fresh printing mixture. *Construction and Building Materials*, 145, 639–647. <https://doi.org/10.1016/J.CONBUILDMAT.2017.04.015>
 39. Khalil, N., Aouad, G., El Cheikh, K., & Rémond, S. (2017). Use of calcium sulfoaluminate cements for setting control of 3D-printing mortars. *Construction and Building Materials*, 157, 382–391. <https://doi.org/10.1016/j.conbuildmat.2017.09.109>
 40. Kim, J. S., Kwon, S. H., Jang, K. P., & Choi, M. S. (2018). Concrete pumping prediction considering different measurement of the rheological properties. *Construction and Building Materials*, 171, 493–503. <https://doi.org/10.1016/j.conbuildmat.2018.03.194>
 41. Kruger, J., Cho, S., Zeranka, S., Viljoen, C., & van Zijl, G. (2020). 3D concrete printer parameter optimisation for high rate digital construction avoiding plastic collapse. *Composites Part B: Engineering*, 183. <https://doi.org/10.1016/j.compositesb.2019.107660>
 42. Laref, R., Losson, E., Sava, A., & Siadat, M. (2019). On the optimization of the support vector machine regression hyperparameters setting for gas sensors array applications. *Chemometrics and Intelligent Laboratory Systems*, 184, 22–27. <https://doi.org/10.1016/J.CHEMOLAB.2018.11.011>
 43. Le, T. T., Austin, S. A., Lim, S., Buswell, R. A., Gibb, A. G. F., & Thorpe, T. (2012). Mix design and fresh properties for high-

- performance printing concrete. *Materials and Structures/Materiaux et Constructions*, 45(8), 1221–1232.
<https://doi.org/10.1617/s11527-012-9828-z>
44. Li, H., Huang, F., Xie, Y., Yi, Z., & Wang, Z. (2017). Effect of water–powder ratio on shear thickening response of SCC. *Construction and Building Materials*, 131, 585–591.
<https://doi.org/10.1016/j.conbuildmat.2016.11.061>
 45. Liu, C., Zhang, R., Liu, H., He, C., Wang, Y., Wu, Y., Liu, S., Song, L., & Zuo, F. (2022a). Analysis of the mechanical performance and damage mechanism for 3D printed concrete based on pore structure. *Construction and Building Materials*, 314.
<https://doi.org/10.1016/j.conbuildmat.2021.125572>
 46. Liu, C., Zhang, R., Liu, H., He, C., Wang, Y., Wu, Y., Liu, S., Song, L., & Zuo, F. (2022b). Analysis of the mechanical performance and damage mechanism for 3D printed concrete based on pore structure. *Construction and Building Materials*, 314.
<https://doi.org/10.1016/j.conbuildmat.2021.125572>
 47. Li, Z., Xingning, L., Conglin, L., bangjun, W., Fanzhang, L., Li, Z., Xingning, L., Conglin, L., bangjun, W., & Fanzhang, L. (2017). National matriculation test prediction based on support vector machines. *JUSTC, 2017, Vol. 47, Issue 1, Pages: 1-9*, 47(1), 1–9.
<https://doi.org/10.3969/J.ISSN.0253-2778.2017.01.001>
 48. Long, W. J., Tao, J. L., Lin, C., Gu, Y. cun, Mei, L., Duan, H. B., & Xing, F. (2019). Rheology and buildability of sustainable cement-based composites containing micro-crystalline cellulose for 3D-printing. *Journal of Cleaner Production*, 239.
<https://doi.org/10.1016/j.jclepro.2019.118054>
 49. Ma, G., Li, Z., & Wang, L. (2018). Printable properties of cementitious material containing copper tailings for extrusion based 3D printing. *Construction and Building Materials*, 162, 613–627.
<https://doi.org/10.1016/j.conbuildmat.2017.12.051>
 50. Ma, G., Li, Z., Wang, L., Wang, F., & Sanjayan, J. (2019). Mechanical anisotropy of aligned fiber reinforced composite for extrusion-based 3D printing. *Construction and Building Materials*, 202, 770–783. <https://doi.org/10.1016/j.conbuildmat.2019.01.008>
 51. Malaeb, Z., AlSakka, F., & Hamzeh, F. (2019). 3D Concrete Printing: Machine Design, Mix Proportioning, and Mix Comparison Between Different Machine Setups. *3D Concrete Printing Technology: Construction and Building Applications*, 115–136.
<https://doi.org/10.1016/B978-0-12-815481-6.00006-3>

52. Manikandan, K., Wi, K., Zhang, X., Wang, K., & Qin, H. (2020). Characterizing cement mixtures for concrete 3D printing. *Manufacturing Letters*, 24, 33–37. <https://doi.org/10.1016/j.mfglet.2020.03.002>
53. Marchment, T., Sanjayan, J., & Xia, M. (2019). Method of enhancing interlayer bond strength in construction scale 3D printing with mortar by effective bond area amplification. *Materials and Design*, 169. <https://doi.org/10.1016/j.matdes.2019.107684>
54. Markin, V., Krause, M., Otto, J., Schröfl, C., & Mechtcherine, V. (2021). 3D-printing with foam concrete: From material design and testing to application and sustainability. *Journal of Building Engineering*, 43. <https://doi.org/10.1016/j.jobbe.2021.102870>
55. Mechtcherine, V., Nerella, V. N., Will, F., Näther, M., Otto, J., & Krause, M. (2019). Large-scale digital concrete construction – CONPrint3D concept for on-site, monolithic 3D-printing. *Automation in Construction*, 107. <https://doi.org/10.1016/j.autcon.2019.102933>
56. Moeini, M. A., Hosseinpour, M., & Yahia, A. (2020). Effectiveness of the rheometric methods to evaluate the build-up of cementitious mortars used for 3D printing. *Construction and Building Materials*, 257. <https://doi.org/10.1016/j.conbuildmat.2020.119551>
57. Mohan, M. K., Rahul, A. V., De Schutter, G., & Van Tittelboom, K. (2021). Early age hydration, rheology and pumping characteristics of CSA cement-based 3D printable concrete. *Construction and Building Materials*, 275. <https://doi.org/10.1016/j.conbuildmat.2020.122136>
58. Nerella, V. N., Krause, M., & Mechtcherine, V. (2020). Direct printing test for buildability of 3D-printable concrete considering economic viability. *Automation in Construction*, 109, 102986. <https://doi.org/10.1016/J.AUTCON.2019.102986>
59. Nerella, V. N., Näther, M., Iqbal, A., Butler, M., & Mechtcherine, V. (2019). Inline quantification of extrudability of cementitious materials for digital construction. *Cement and Concrete Composites*, 95, 260–270. <https://doi.org/10.1016/j.cemconcomp.2018.09.015>
60. Nessim, A. A., & Wajda, R. L. (2015). The rheology of cement pastes and fresh mortars. *https://Doi.Org/10.1680/Macr.1965.17.51.59*, 17(51), 59–68. <https://doi.org/10.1680/MACR.1965.17.51.59>

61. Nguyen, V. H., Remond, S., & Gallias, J. L. (2011). Influence of cement grouts composition on the rheological behaviour. *Cement and Concrete Research*, 41(3), 292–300. <https://doi.org/10.1016/J.CEMCONRES.2010.11.015>
62. Panda, B., Mohamed, N. A. N., Paul, S. C., Singh, G. V. P. B., Tan, M. J., & Šavija, B. (2019). The effect of material fresh properties and process parameters on buildability and interlayer adhesion of 3D printed concrete. *Materials*, 12(13). <https://doi.org/10.3390/ma12132149>
63. Panda, B., & Tan, M. J. (2019). Rheological behavior of high volume fly ash mixtures containing micro silica for digital construction application. *Materials Letters*, 237, 348–351. <https://doi.org/10.1016/j.matlet.2018.11.131>
64. Paolo, F., Mantia, L., Dri, N. ', Konan, A., Rosenbaum, E., & Massoudi, M. (2022). On the Response of a Herschel–Bulkley Fluid Due to a Moving Plate. *Polymers* 2022, Vol. 14, Page 3890, 14(18), 3890. <https://doi.org/10.3390/POLYM14183890>
65. Papachristoforou, M., Mitsopoulos, V., & Stefanidou, M. (2018). Evaluation of workability parameters in 3D printing concrete. *Procedia Structural Integrity*, 10, 155–162. <https://doi.org/10.1016/j.prostr.2018.09.023>
66. Papo, A. (1988). Rheological models for cement pastes. *Materials and Structures*, 21(1), 41–46. <https://doi.org/10.1007/BF02472527/METRICS>
67. (PDF) *Rheological method to evaluate structural buildup in self-consolidating concrete cement pastes*. (n.d.). Retrieved 19 May 2025, from https://www.researchgate.net/publication/235269207_Rheological_method_to_evaluate_structural_buildup_in_self-consolidating_concrete_cement_pastes
68. Perrot, A., Rangeard, D., & Pierre, A. (2016). Structural built-up of cement-based materials used for 3D-printing extrusion techniques. *Materials and Structures/Materiaux et Constructions*, 49(4), 1213–1220. <https://doi.org/10.1617/s11527-015-0571-0>
69. Pham, L., Tran, P., & Sanjayan, J. (2020). Steel fibres reinforced 3D printed concrete: Influence of fibre sizes on mechanical performance. *Construction and Building Materials*, 250. <https://doi.org/10.1016/j.conbuildmat.2020.118785>
70. Rahul, A. V., Mohan, M. K., De Schutter, G., & Van Tittelboom, K. (2022). 3D printable concrete with natural and recycled coarse

- aggregates: Rheological, mechanical and shrinkage behaviour. *Cement and Concrete Composites*, 125. <https://doi.org/10.1016/j.cemconcomp.2021.104311>
71. Rahul, A. V., Santhanam, M., Meena, H., & Ghani, Z. (2019a). 3D printable concrete: Mixture design and test methods. *Cement and Concrete Composites*, 97, 13–23. <https://doi.org/10.1016/J.CEMCONCOMP.2018.12.014>
 72. Rahul, A. V., Santhanam, M., Meena, H., & Ghani, Z. (2019b). 3D printable concrete: Mixture design and test methods. *Cement and Concrete Composites*, 97, 13–23. <https://doi.org/10.1016/j.cemconcomp.2018.12.014>
 73. Rahul, A. V., Santhanam, M., Meena, H., & Ghani, Z. (2019c). Mechanical characterization of 3D printable concrete. *Construction and Building Materials*, 227, 116710. <https://doi.org/10.1016/J.CONBUILDMAT.2019.116710>
 74. Ren, Q., Li, M., Zhang, M., Shen, Y., & Si, W. (2019). Prediction of Ultimate Axial Capacity of Square Concrete-Filled Steel Tubular Short Columns Using a Hybrid Intelligent Algorithm. *Applied Sciences* 2019, Vol. 9, Page 2802, 9(14), 2802. <https://doi.org/10.3390/APP9142802>
 75. Rheology of Fresh Cement and Concrete. (1991). *Rheology of Fresh Cement and Concrete*. <https://doi.org/10.4324/9780203473290>
 76. Roussel, N. (2005). Steady and transient flow behaviour of fresh cement pastes. *Cement and Concrete Research*, 35(9), 1656–1664. <https://doi.org/10.1016/J.CEMCONRES.2004.08.001>
 77. Schultz, M. A., & Struble, L. J. (1993). Use of oscillatory shear to study flow behavior of fresh cement paste. *Cement and Concrete Research*, 23(2), 273–282. [https://doi.org/10.1016/0008-8846\(93\)90092-N](https://doi.org/10.1016/0008-8846(93)90092-N)
 78. Struble, L. J., & Schultz, M. A. (1993). Using creep and recovery to study flow behavior of fresh cement paste. *Cement and Concrete Research*, 23(6), 1369–1379. [https://doi.org/10.1016/0008-8846\(93\)90074-J](https://doi.org/10.1016/0008-8846(93)90074-J)
 79. Sun, C., Xiang, J., Xu, M., He, Y., Tong, Z., & Cui, X. (2020). 3D extrusion free forming of geopolymer composites: Materials modification and processing optimization. *Journal of Cleaner Production*, 258. <https://doi.org/10.1016/j.jclepro.2020.120986>
 80. Suntharalingam, T., Nagaratnam, B., Poologanathan, K., Hackney, P., & Ramli, J. (n.d.). *EFFECT OF POLYPROPYLENE FIBRES ON*

THE WORKABILITY PARAMETERS OF EXTRUDABLE CEMENTITIOUS MATERIALS.

81. Tarhan, Y., & Şahin, R. (2021a). Fresh and rheological performances of air-entrained 3d printable mortars. *Materials*, 14(9). <https://doi.org/10.3390/ma14092409>
82. Tarhan, Y., & Şahin, R. (2021b). Fresh and Rheological Performances of Air-Entrained 3D Printable Mortars. *Materials* 2021, Vol. 14, Page 2409, 14(9), 2409. <https://doi.org/10.3390/MA14092409>
83. Uddin, M. N., Ye, J., Deng, B., Li, L. zhi, & Yu, K. (2023). Interpretable machine learning for predicting the strength of 3D printed fiber-reinforced concrete (3DP-FRC). *Journal of Building Engineering*, 72, 106648. <https://doi.org/10.1016/J.JOBE.2023.106648>
84. Van Der Putten, J., De Schutter, G., & Van Tittelboom, K. (2019). Surface modification as a technique to improve inter-layer bonding strength in 3d printed cementitious materials. *RILEM Technical Letters*, 4, 33–38. <https://doi.org/10.21809/rilemtechlett.2019.84>
85. Wang, W., Konstantinidis, N., Austin, S. A., Buswell, R. A., Cavalaro, S., & Cecinia, D. (2020). Flexural Behaviour of AR-Glass Textile Reinforced 3D Printed Concrete Beams. In *RILEM Bookseries* (Vol. 28, pp. 728–737). Springer. https://doi.org/10.1007/978-3-030-49916-7_73
86. Xiao, J., Zou, S., Yu, Y., Wang, Y., Ding, T., Zhu, Y., Yu, J., Li, S., Duan, Z., Wu, Y., & Li, L. (2020). 3D recycled mortar printing: System development, process design, material properties and on-site printing. *Journal of Building Engineering*, 32. <https://doi.org/10.1016/j.job.2020.101779>
87. Xu, J., Ding, L., Cai, L., Zhang, L., Luo, H., & Qin, W. (2019). Volume-forming 3D concrete printing using a variable-size square nozzle. *Automation in Construction*, 104, 95–106. <https://doi.org/10.1016/j.autcon.2019.03.008>
88. Xu, Y., Schlangen, E., & Šavija, B. (2020). Auxetic Behavior of Cementitious Cellular Composites Under Uniaxial Compression and Cyclic Loading. In *RILEM Bookseries* (Vol. 28, pp. 547–556). Springer. https://doi.org/10.1007/978-3-030-49916-7_56
89. Xu, Y., Yuan, Q., Li, Z., Shi, C., Wu, Q., & Huang, Y. (2021). Correlation of interlayer properties and rheological behaviors of 3DPC with various printing time intervals. *Additive Manufacturing*, 47. <https://doi.org/10.1016/j.addma.2021.102327>

90. Zareiyan, B., & Khoshnevis, B. (2017). Interlayer adhesion and strength of structures in Contour Crafting - Effects of aggregate size, extrusion rate, and layer thickness. *Automation in Construction*, 81, 112–121. <https://doi.org/10.1016/j.autcon.2017.06.013>
91. Zhang, D., Qian, L., Mao, B., Huang, C., Huang, B., & Si, Y. (2018). A Data-Driven Design for Fault Detection of Wind Turbines Using Random Forests and XGboost. *IEEE Access*, 6, 21020–21031. <https://doi.org/10.1109/ACCESS.2018.2818678>
92. Zhang, Y., Zhang, Y., She, W., Yang, L., Liu, G., & Yang, Y. (2019). Rheological and harden properties of the high-thixotropy 3D printing concrete. *Construction and Building Materials*, 201, 278–285. <https://doi.org/10.1016/j.conbuildmat.2018.12.061>
93. Zhou, T., Lu, H., Wei, X., & Xia, Y. (2017). Self-adaption fusion algorithm for lung cancer PET/CT based on Piella frame and DT-CWT. *Journal of University of Science and Technology of China*, 47(1), 10–17. <https://doi.org/10.3969/J.ISSN.0253-2778.2017.01.002>
94. Li, H., Lin, J., Lei, X., & Wei, T. (2022). Compressive strength prediction of basalt fiber reinforced concrete via random forest algorithm. *Materials Today Communications*, 30, 103117. <https://doi.org/10.1016/J.MTCOMM.2021.103117>
95. Yuan, X., Tian, Y., Ahmad, W., Ahmad, A., Usanova, K. I., Mohamed, A. M., & Khallaf, R. (2022). Machine Learning Prediction Models to Evaluate the Strength of Recycled Aggregate Concrete. *Materials*, 15(8), 2823. <https://doi.org/10.3390/MA15082823/S1>
96. Zhang, D., Qian, L., Mao, B., Huang, C., Huang, B., & Si, Y. (2018). A Data-Driven Design for Fault Detection of Wind Turbines Using Random Forests and XGboost. *IEEE Access*, 6, 21020–21031. <https://doi.org/10.1109/ACCESS.2018.2818678>

